Crystal chemistry and partitioning of halogens in hydrous silicates

Sarah Figowy, Benoît Dubacq, Philippe d'Arco

Crystal chemistry and partitioning of halogens in hydrous silicates

Sarah Figowy[1], Benoît Dubacq[1], Philippe D'Arco[1]

[1]Sorbonne Université, CNRS-INSU, Institut des Sciences de la Terre de Paris, ISTeP UMR 7193, F-75005 Paris, France

Correspondence to: Sarah Figowy (sarah.figowy@sorbonne-universite.fr)

Abstract.
Understanding how halogens are distributed among usual hydrous silicates in the lithosphere is important to constrain their deep geochemical cycle and fluid-rock interactions in subduction zones. This article presents first-principles modelling of halogen (F^-, Cl^-, Br^-) incorporation in hydrous silicates including mica, chlorite, serpentine, amphibole, epidote and carpholite. The approach allows studying the impact of crystal chemistry on halogen partitioning by quantification of the energetic cost of halogen incorporation in minerals. Calculations are carried out in large systems where halogens are in minor to trace concentrations. Estimations show that F-bearing defects must be separated at least 9 Å from one another to reproduce trace element behaviour, this value increasing to at least 10 Å for Cl and Br. Results highlight the competition between the effects of electrostatic interactions and steric hindrance for incorporation of halogens, where steric hindrance has greater importance for heavy halogens, in particular for Br. Interaction with alkalis is a major control for F incorporation, especially in mica. Other parameters such as octahedral site occupancy, Si/Al ratio of tetrahedral sites and the nature of alkalis in amphibole and mica (K or Na) appear to play subordinate roles. Partition coefficients have been estimated in mineral assemblages in an effort to be representative of subduction zone metamorphism. Results show that pargasite, biotite and lizardite are favoured hosts for all three halogens, followed by clinochlore, tremolite and carpholite. The energetic cost of incorporating halogens into dioctahedral phyllosilicates and epidote is comparatively higher, and partitioning is predicted as unfavourable to these minerals. Fractionation between halogens in subduction zones is predicted by the evolution of mineral assemblages and partition coefficients, a consequence of the influence of crystal chemistry over halogen incorporation in hydrous silicates.

Keywords: Halogens; Partition coefficient; Crystal chemistry; *ab initio*; first-principles calculations; CRYSTAL

Declarations.
Funding. The present work has been funded by the Tellus SYSTER programs of CNRS-INSU and by ISTeP. Computing time was awarded on the MeSU (Sorbonne Université) and CINES calculation centres.

Competing interests. The authors have no financial or proprietary interests in any material discussed in this article.

Availability of data and material. Not applicable.

Code availability. Not applicable.

Acknowledgments.
The authors are indebted to the MeSU (Sorbonne Université) and CINES calculation centres. Benoît Villemant, Étienne Balan and Olivier Namur are thanked for fruitful discussions. Two anonymous reviewers are gratefully acknowledged for their constructive comments.

Introduction

Halogens (F, Cl, Br and I) play an important role in Earth's atmosphere, hydrosphere and biosphere, from catalysers of ozone breakdown to vital components of thyroid hormones in humans. The long-term cycle of halogens is profoundly controlled by plate tectonics, as for other volatiles abundantly found in the lithosphere such as water, carbon dioxide and sulfur. A major divergence takes place in subduction zones: volatiles travel back to the surface via arc volcanism or (re-)enter the deep mantle (e.g. Zellmer et al. 2015; Allègre et al. 1977), with vast implications for the atmosphere, climate, habitability as well as for the rheologic and melting properties of deep rocks. The behaviour of volatiles in subduction zones is multifold and complex, via several competing processes acting on reservoirs in the subducting plate, mantle wedge and crust. Subducted metamorphosed mafic and pelitic rocks carry volatile elements to the deep mantle to various extents (Angiboust and Agard 2010; Smye et al. 2013) depending on variations in stability and volatile content of minerals such as amphibole, lawsonite and phyllosilicates (mostly chlorite, mica and serpentine). Presence of halogens may increase the stability of biotite and amphibole, enhance the transport of metallic elements via complexation (Seward et al. 2014) and alter the pH of subduction fluids (Galvez et al. 2016). In this context, understanding and quantifying the incorporation of halogens in minerals is paramount to modelling their geochemical cycle (see Siron et al. 2018; Barnes et al. 2019) and its effects. Halogens are commonly major components of accessory phases such as apatite and tourmaline, and they are hosted in minor to trace amounts in hydrous silicates such as micas, amphibole and serpentine (e.g. Westrich 1982; Chevychelov et al. 2008; Pagé et al. 2016; Mi and Pan 2018) that are ubiquitous in the continental and oceanic crust. The overall abundance of hydrous silicates grants them a role in the storage and transport of halogens, especially in subduction zones.

Yet there is little information about halogen partitioning in most hydrous silicates, especially for Br and I (e.g. Hanley and Koga 2018). Most of the current data cover the partitioning of F and to a lesser extent that of Cl in biotite, serpentine and amphibole. Halogens are known to be incorporated into the crystal structure of hydrous silicates through the homovalent exchange $X^- = OH^-$, where $X^- = F^-$, Cl^-, Br^- or I^- (e.g. Oberti 1993; Robert et al. 1993). As the ionic radius of F^- is close to that of the hydroxyl group (1.33 Å for F^- and 1.37 Å for OH^-, all radii in this article are from Shannon 1976), F is the most compatible halogen in hydrated silicates and often the most abundant in silicates due to terrestrial ratios (for 1 F: ~ 0.5 Cl, ~ $2.6*10^{-3}$ Br, ~ $5*10^{-4}$ I, after Hanley and Koga 2018). Heavier halogens Cl^- (1.81 Å), Br^- (1.96 Å) and I^- (2.20 Å) are far more incompatible in silicates due to their large ionic radius but are frequently hosted at trace amounts. For example, Teiber et al. (2015) reported up to 1.5 ppm of Br in biotite, and several hundreds of ppb of Br in amphibole.

Halogen uptake in minerals is partly controlled by external factors such as pressure-temperature conditions or fluid composition (Teiber et al. 2015), and partly by crystal chemical parameters. The chemical composition of the host mineral exerts a control over halogen partitioning with fluids (see e.g. the K-Cl correlation of Morrison (1991), in amphibole, and Henry and Dutrow (2011) for F in tourmaline). In mica, the Mg/Fe/Al content of the octahedral sheet modifies F and Cl incorporation (e.g. Volfinger et al. 1985; Robert et al. 1993; Henry and Daigle 2018). Correlations and anti-correlations between major elements with F and Cl have been found in several studies, leading to the hypothesis of Fe-F avoidance and Mg-Cl avoidance (e.g. Chevychelov et al. 2008; Aranovich and Safonov 2018), although some authors obtained discordant results (Siron et al. 2018; Heckel et al. 2020), possibly due to threshold effects in halogen concentration (Daigle 2015).

The low abundance of halogens in silicates makes *in situ* analysis difficult as detection limits are often too high (Hammerli and Rubenach 2018). Bulk analyses may be carried out for F, Cl and Br (see Pagé et al. (2018) for serpentinites) but point analyses are needed to constrain partitioning between minerals. Experimental approaches provided fluid/mineral and melt/mineral partition coefficients for halogens, but data on mineral/mineral partitioning remain scarce (see e.g. Westrich 1982), and halogens are often introduced at concentrations well above natural amounts, with the consequence that strain fields around halogen-bearing sites interact with each other. The obtained partition coefficients may therefore depend on halogen concentration and not reflect partitioning in natural settings.

First-principles calculation of mineral/fluid partitioning is also difficult as modelling trace elements in fluid phases is very challenging, requiring thermodynamic integration (e.g. Wagner et al. 2017) in systems containing hundreds if not thousands of atoms. Recent modelling studies quantified the partitioning of trace cations between minerals (see Dubacq and Plunder 2018; Figowy et al. 2020) together with the structural strain after exchange reactions. This approach has been selected to study the incorporation of trace amounts of halogens in widespread hydrous silicates and their partitioning, with emphasis on quantifying the influence of crystal chemistry. This has been carried out by 1)

comparing the energetic cost of halogen incorporation through OH^- exchange between minerals and between crystal sites, 2) quantifying the role of site occupancy, ionic interactions and steric hindrance (i.e. the *local* strain induced by the halogen-bearing defect) on halogen distribution, and 3) computing partition coefficients between phases in representative assemblages.

Protocol: first-principles modelling of exchange reactions

The $X^- = OH^-$ exchange is modelled using CRYSTAL17. A complete technical description of the program may be found in Dovesi et al. (2005) and Dovesi et al. (2014). The methodology for the study of trace elements is described briefly here and provided in greater details in Dubacq and Plunder (2018) and Figowy et al. (2020). Crystal structures have been optimised using the hybrid B3LYP functional, first in halogen-free minerals, then after exchange of a hydroxyl group with F, Cl or Br. Due to computational limits, iodine has not been modelled here. The ground-state energy was optimised following a self-consistent field algorithm until satisfying a threshold value of 10^{-8} Ha between two cycles of the iterative procedure. A second optimisation procedure was carried out to find the optimal structure, ending when four convergence criteria were satisfied (in arbitrary units of CRYSTAL17): maximum energy gradient (0.00045), RMS gradient (0.0003), maximum atom displacement (0.0018) and associated RMS (0.0012). Details about the CRYSTAL17 keywords are provided in Online Resource 5. The basis sets used here originate from: Nada et al. (1993) for F, Aprà et al. (1993) for Cl, Peintinger et al. (2012) for Br, Dovesi et al. (1983) for H, Valenzano et al. (2006) for O and Ca, Dovesi et al. (1991) for Na, McCarthy and Harrison (1994) for Mg, Catti et al. (1994) for Al, D'Arco et al. (1993) for Si, Civalleri et al. (2003) for K, Towler et al. (1994) for Mn, Catti et al. (1995) for Fe.

The procedure minimises the energy of the system and yields atomic positions as well as cell parameters for each hydrous silicate and their halogen-bearing counterpart. This allows quantification of strain around the halogen-bearing defect, and extraction of the energy difference after the $X^- = OH^-$ exchange in each phase, expressed per mole of halogen ion and coined "defect energy" as in Allan et al. (2003). Equation 1 yields the defect energy $U_d^{\text{F-Tlc}}$ for incorporation of F in talc where $E_{\text{F-Tlc}}$ is the optimised energetic level of F-bearing talc (i.e. after $F^- = OH^-$ exchange):

$$U_d^{\text{F-Tlc}} = E_{\mathbf{F}\text{-Tlc}} - E_{\text{Tlc}} \quad (1)$$

Comparing defect energies allows estimating the Gibbs free energy of exchange reactions, as exemplified below for an exchange between talc and pyrophyllite (reaction R1). F-Prl and F-Tlc are fluorine-bearing pyrophyllite and talc. This example is selected for simplicity as both phases contain only one independent OH site per formula unit. The expression becomes cumbersome for minerals with multiple independent exchange sites, as discussed further.

$$\text{F-Prl} + \text{Tlc} = \text{F-Tlc} + \text{Prl} \quad (R1)$$

The corresponding Gibbs free energy of reaction is assumed equal to the difference between the computed defect energies (see Dubacq and Plunder 2018; Figowy et al. 2020):

$$\Delta G_r^{\circ}{}_{\text{R1}} = U_d^{\text{F-Tlc}} - U_d^{\text{F-Prl}} \quad (2)$$

It is noted that this procedure does not account for variations of entropy, which are assumed negligible compared to enthalpy variations in exchange reactions for trace elements, and does not depend on pressure or temperature. Pressure dependency is very small over lithospheric depths for any given mineral assemblage. Temperature dependency is included during calculations of the partition coefficient obtained from the Gibbs free energy of reaction through the reaction constant K:

$$\text{K} = \frac{x_{\text{F}}^{\text{Tlc}} * x_{\text{OH}}^{\text{Prl}}}{x_{\text{F}}^{\text{Prl}} * x_{\text{OH}}^{\text{Tlc}}} = \frac{D_{\text{F}}^{\text{Tlc/Prl}}}{D_{\text{OH}}^{\text{Tlc/Prl}}} \quad (3)$$

$$D_{\text{F}}^{\text{Tlc/Prl}} = \frac{x_{\text{OH}}^{\text{Prl}}}{x_{\text{OH}}^{\text{Tlc}}} . \exp\left(\frac{-\Delta G_r^{\circ}{}_{\text{R1}}}{\text{R}T}\right) \quad (4)$$

where $x_{\text{F}}^{\text{Tlc}}$ is the fraction of F effectively in talc, and so on. R is the gas constant. It is implicit in these equations that the dilute limit is approached and that mineral end-members have activity coefficient ratios equal to one. For minerals with several independent OH sites such as phlogopite and pargasite, the contribution of each site to the overall partition coefficient is accounted for by summation, after $X^- = OH^-$ exchange and optimisation are individually carried out on each site. An example is worked out in the "Halogen partitioning" part.

It is noteworthy that with varying pressure-temperature conditions, different mineral assemblages arise and therefore this procedure provides representative partition coefficients for various metamorphic grades.

At trace amounts, defects are supposed sufficiently far from one another to avoid interaction between their strain fields (see for example Carpenter et al. 2009), leading to a mixing regime where defect energy (and therefore Eq. 3) are independent of concentration. In

order to reproduce trace element behaviour for halogen-bearing defects, the halogen for OH substitutions have been carried out using various supercells built from the primitive cell, generated over the three dimensions (see Table 1). The choice of the largest supercell is dictated by the computational resources and by the converged character of the Gibbs free energy as described in the following section. It is noted that the use of supercells lifts space group constraints, effectively allowing strain around the defect. Supercells are also needed to reproduce "Al avoidance" (see Dove et al. (1996) among others) in ordered minerals such as micas. Al avoidance has been described as effective up to temperatures above the stability field of most phyllosilicates (see e.g. Palin et al. 2001), allowing a more homogeneous distribution of charges. A consequence of the use of supercells is the appearance of independent sites, linked to the loss of space group constraints. For example, in phlogopite, four independent OH-bearing sites are found in the 2×2×1 replicate of the original unit cell of Pabst et al. (1955, with only one OH site). This implies testing halogen incorporation in every one of them.

Results

Table 1 lists cell parameters obtained after optimisation together with experimentally-derived structures. Mineral abbreviations originate from Whitney and Evans (2010), with the addition of "Asp" for aspidolite and "Pis" for the pistacite component of epidote (hereafter referred to as pistacite $Ca_2Fe^{3+}{}_3(SiO_4)(Si_2O_7)O(OH)$).

Brucite: a test for trace-element behaviour

Brucite has been chosen as a proxy for phyllosilicate structures to evaluate the approximate system size necessary to reach trace-element behaviour. This choice is motivated by the small cell size of brucite, allowing several replications in all directions before being hampered by computational limits.

Figure 1 shows the evolution of the enthalpy of reaction R2 as a function of the halogen content in the simulation, written below for F.

$$Mg(OH)_2 + \frac{1}{2}F_2 = Mg(OH)F + \frac{1}{2}O_2 + \frac{1}{2}H_2 \qquad (R2)$$

In reaction R2, $Mg(OH)_2$ and F-bearing brucite have been optimised as described above. F_2, O_2 and H_2 have been modelled as molecules. The enthalpy of reaction generally increases with increasing dilution, until stabilizing so that the energy difference between two supercells becomes negligible (below 1 $kJ.mol^{-1}$, left of the dotted line). Defect energies reflect this evolution without the need of evaluating the energetic state of F_2, O_2 and H_2 in reaction R2. For the $F^- = OH^-$ exchange, the enthalpy of reaction appears to stabilize around -8 $kJ.mol^{-1}$ with dilution levels where halogen defects are separated from each other by ~ 9 Å (Fig. 1A). Enthalpies computed for Cl and Br begin to stabilize at higher dilution, corresponding to distances in the range of 10-12 Å (Fig 1C-E). Convergence of the reaction enthalpies is linked to that of lattice-scale strain, as approximated by cell volume variations (Fig. 1B-D-F). Ideally, cell strain after incorporation of a trace element would be zero, as for a point defect in an infinitely-large crystal. Convergence is well illustrated by the brucite example: the absolute value of cell strain remains above zero in the most dilute cases for all three halogens, but the remaining energetic variations are very small. These results support application of the method to model trace-element incorporation and to estimate partition coefficients. It is noteworthy that required dilution levels depend on the halogen and on the host mineral because strain fields vary (see Dubacq and Plunder 2018). In any case, the behaviour of halogens in brucite highlights the need for dilution (and therefore using large systems with supercells) to reach a constant enthalpy of reaction and obtain meaningful information for strain around defects corresponding to trace-element behaviour, at the price of increased computational cost. A compromise between high dilution level and reasonable number of atoms has been necessary for each crystal structure studied below.

Optimised structures

The Online Resource 1 provides optimised energies and cell parameters for each phase modelled here (see Table 1 for end-members). Each independent OH site has been tested for exchange with halogens. These sites are displayed in Figure 2 for phlogopite (Fig. 2A), muscovite (Fig. 2B), lizardite (Fig. 2C), kaolinite (Fig. 2D), clinochlore (Fig. 2E), sudoite (Fig. 2F), pargasite (Fig. 2G) and Mg-carpholite (Fig. 2H) in order to highlight structural characteristics also found in other minerals. The number of minerals allows testing for several crystal chemical parameters, among which steric hindrance, composition of the octahedral layer and that of interlayer space in phyllosilicates. Hereafter, each OH site is labelled with the mineral abbreviation as exponent (i.e. $OH1^{Kln}$ is the OH1 site of kaolinite, $F\text{-}OH1^{Kln}$ after $F^- = OH^-$ substitution). Modelled minerals – with the exception of lizardite – display cell volumes slightly larger than experimental ones (Table 1), with volume variations globally lower than 6 %. This increase is expected from the use of the B3LYP functional which is

known to overestimate cell volumes (e.g. De La Pierre et al. 2016). Talc and pyrophyllite display a volume increase of ~ 7.5 %, due to their structure being easily strained along the *c*-axis. The optimised cell volume of lizardite is surprisingly almost identical to that of the experimental reference (less than 1 ‰ of volume variation).

Phyllosilicates are divided in two groups here: dioctahedral and trioctahedral. In trioctahedral species, three sites out of three are occupied by cations, but only two sites are filled in dioctahedral phyllosilicates, the last site being vacant. This causes a deviation of the OH orientation in dioctahedral phyllosilicates, which tends to parallel the octahedral plane, pointing towards the vacancy, whereas OH is almost perpendicular to the sheet plane in trioctahedral sheets (compare e.g. Fig. 2A-B). This difference has been described in previous studies (see Giese 1975, 1977; Bookin and Drits 1982; Munoz 1984, among others).

Micas (Fig. 2A-B) are T-O-T phyllosilicates with a positively charged interlayer space containing K^+ (muscovite and phlogopite) or Na^+ (paragonite and aspidolite). Selected space groups C2/m and C2/c correspond to the experimentally well-constrained 1M and 2M1 polytypes (e.g. Giese 1977), the most abundant in natural trioctahedral and dioctahedral micas, respectively. Each supercell of mica includes four independent OH sites. Due to Al avoidance, $OH4^{Phl}$ and $OH3^{Ms}$ are located between six Si atoms, whereas other OH groups are neighboured by four Si and two Al atoms.

Lizardite and kaolinite (Fig. 2C-D) are T-O phyllosilicates with empty interlayer space. In lizardite, $OH2^{Lz}$ is oriented towards the octahedral layer, $OH1^{Lz}$ points towards the interlayer space. Kaolinite has four independent OH sites as the octahedral vacancy deviates hydroxyl groups. $OH1^{Kln}$ is in the T-O sheet, and the three others are pointing toward the interlayer.

Talc and pyrophyllite are T-O-T phyllosilicates with a non-charged interlayer space and only one OH site. $OH1^{Tlc}$ is oriented toward the interlayer space, whereas $OH1^{Prl}$ is pointing toward the octahedral vacancy.

Chlorite is a T-O-T-O phyllosilicate where the mica-like T-O-T sheet encloses a brucite-like layer. Two chlorite types have been considered: a tri-trioctahedral clinochlore (Fig. 2E) and a di-trioctahedral sudoite (Fig. 2F), both with ten independent OH sites. The first three are located in the T-O-T sheet, and the others belong to the interlayer brucite-like sheet.

Two amphibole types, pargasite (Fig. 2G) and tremolite, have been included in the modelling. In amphibole, OH groups are oriented towards the A-site, almost perpendicularly to the octahedral and tetrahedral planes. The A-site is occupied by Na in pargasite, but vacant in tremolite. One out of four tetrahedral sites in pargasite is occupied by Al. This leads to four independent OH sites: $OH1^{Prg}$, $OH2^{Prg}$ and $OH4^{Prg}$ are neighboured by four Si and two Al atoms, whereas $OH3^{Prg}$ is only surrounded by Si atoms. Tremolite has higher symmetry with tetrahedral sites fully occupied by Si^{4+} and only one independent OH site.

Epidote is a sorosilicate with the formula $A_2M_3[T_2O_7][TO_4]O(OH)$, where A-sites are mostly filled with Ca, less commonly by Mn, Ba or rare earths. M-sites are occupied by trivalent cations and T-sites mostly by Si. There is only one OH site, bridging tetrahedral and octahedral sites. The structures of clinozoisite and pistacite have been selected, the main difference between the two is that Fe^{3+} in pistacite replaces Al of clinozoisite. As no structure refinement was available for pistacite, the structure of clinozoisite in which all Al have been replaced by Fe^{3+} has been used as geometrical guess.

Carpholite is an inosilicate with ideal formula $MnSi_2Al_2O_6(OH)_4$, and two large OH sites in a cage structure. $OH1^{Car}$ is bonded to 1 Al and 1 Mn, and $OH2^{Car}$ is bonded to 2 Al and 1 Mn. Mg-carpholite $MgSi_2Al_2O_6(OH)_4$ shows the same structure and is abundantly found in metapelite of the blueschist facies, exposed to high-pressure and low-temperature conditions (see Agard et al. 2005). Both minerals have been modelled here.

Strain

Halogen-bearing defects must be diluted to reproduce trace element behaviour. In such ideal system, the strain induced by halogen incorporation should be localised around the defect, and the strain at the scale of the cell should be of zero, as for the brucite case (Fig. 1).

The Online Resource 2 displays strain at cell scale due to halogen incorporation. Structures are deformed with both axial and angular strain, below 3‰ for all phases in the case of $F^- = OH^-$ exchange. For Cl and Br, the strain on *a* and *b* axes is smaller than 1 %. The largest strains affect the *c* axis for $OH4^{Kln}$ (1.5 % for Cl = OH exchange and 1.2 % for Br = OH exchange) and for $OH2^{Lz}$ (1.8 % for Br = OH exchange). Angular strains are limited too, mostly below 2 %. In all cases, strain at cell-scale is very small, consistently with results in brucite. In pargasite, the distance between two defect-bearing OH sites is modified by ~ -0.8 ‰ for F, +0.1-0.2 % for Cl and +0.3-0.4 % for Br, whereas it is of ~ -0.5 ‰ for F, +0.2 % for Cl and +0.3 % for Br in tremolite. Most of the strain is accommodated in the direct environment of the defect and interactions between the strain fields around halogen defects appear all but negligible. The main message of these results is that the limited strain at cell scale is consistent with trace element modelling.

Figure 3 displays the computed *local* strain (in %) due to halogen incorporation in phlogopite (3A, 3B, 3C) and in talc (3D, 3E, 3F). The interlayer distance variation between two oxygen atoms is also indicated, as well as the <K-X> distance variation in phlogopite, with X the halogen.

Angular strain is very small in phlogopite and talc. For the $F^- = OH^-$ exchange, bond strain is small, with F-Si, F-Al and F-Mg distances slightly larger than the original OH-Si, OH-Al and OH-Mg distances in phlogopite (from +0.3 %, +0.6 % and +0.5 %, respectively). The disturbance is larger in talc, with an increase of ~ +1.1 % and +1.9 % for F-Si and F-Al, and a decrease of -0.8 % for F-Mg. For both minerals, the heavier the halogen, the larger the local strain. Distances between Cl or Br and tetrahedral cations are smaller than with the original OH site, with comparable decreases in phlogopite and talc. Conversely, the distance between Cl or Br and Mg is larger than the original, from +11 % (Cl) and +14 % (Br) up to +23 % (Cl) and +27 % (Br) in phlogopite. Cl and Br are displaced away from the octahedral sheet towards the interlayer space.

The main difference between halogen incorporation in talc and phlogopite is observed along the *c* axis. The interlayer space increases slightly due to Cl and Br incorporation in talc, but not for F. In phlogopite, the interlayer space decreases slightly for all halogens. The distance between K and Cl or Br decreases by -20 %.

Figure 4 displays the strain around halogen defects in tremolite (4A, 4B, 4C) and pargasite (4D, 4E, 4F). For pargasite, only strains around $OH2^{Prg}$ (surrounded by Si and tetrahedral Al, bottom of Fig. 4D-E-F) and $OH3^{Prg}$ (surrounded by Si only, top of Fig. 4D-E-F) are compared here for readability. There is no clear difference in strain between these two sites. As for talc and phlogopite, the local strain depends on the nature of the incorporated halogen. In tremolite, the Ca-F distance is 0.9% longer than the original Ca-O distance, whereas the F-Mg bond is shorter (Fig. 4A). In pargasite, where the A-site is occupied by Na, the Ca-F distance is similarly larger, but the F-Mg distance is 1.1% longer than O-Mg (Fig. 4D). The Na-F length is 11% smaller than the original Na-O, a larger value than for K-F strain in phlogopite (Fig. 3A).

For the $Cl^- = OH^-$ exchange (Fig. 4B-E), strain is larger, as in talc and phlogopite. The distance between the oxygen of the OH site and Mg is increased similarly in both amphiboles by ~ +20 % after Cl incorporation. The Cl atom is displaced from the OH site, slightly more so in pargasite than in tremolite. The Ca-Cl distance is smaller than the original, by -5.9 % in pargasite and -5.5 % in tremolite. In pargasite, the distance between Na and the halogen-filled OH site is strongly reduced by -27 % in $OH3^{Prg}$, and -23 % in $OH2^{Prg}$.

For the $Br^- = OH^-$ exchange (Fig. 4C-F), strain is systematically larger. The distance between Mg and the halogen-filled OH site increases identically by +25 % in tremolite and pargasite after Br incorporation. The Ca-Br distance is smaller than the original Ca-O distance, also similarly in both amphiboles. Angular strain is limited, showing slight differences of ±1 % between $OH3^{Prg}$ and $OH2^{Prg}$ local environment. Interestingly, the distance decrease between Na and the incorporation site in pargasite is less important than in the case of Cl uptake. Compared with phyllosilicates, the accommodation of strain in amphiboles is less anisotropic.

Gibbs free energy of $X^- = OH^-$ exchanges

Figure 5 shows the differences in defect energies for all structures. The Gibbs free energy corresponding to the $X^- = OH^-$ exchange reactions between the $OH1^{Phl}$ site of phlogopite and each independent site of every mineral is shown on the right-hand site (in $kJ.mol^{-1}$). For example, reaction R3 corresponds to the halogen exchanges between $OH1^{Phl}$ and $OH2^{Prg}$. These reactions can be directly transposed to other sites, other structures and other halogens ($\measuredangle G_r°_{R4}$ for the $Cl^- = OH^-$ exchange, $\measuredangle G_r°_{R5}$ for the $Br^- = OH^-$ exchange).

$$\text{F-OH1}^{\text{Phl}} + \text{OH2}^{\text{Prg}} = \text{F-OH2}^{\text{Prg}} + \text{OH1}^{\text{Phl}} \qquad \text{(R3)}$$

A positive value for the Gibbs energy of reaction in Fig. 5 designates $OH1^{Phl}$ as the favoured host site for halogen, and inversely a negative value shows the other site is energetically more favourable. A large absolute value for the Gibbs energy of reaction implies a large partition coefficient, due to the exponential dependency in Eq. 4. Figure 5 allows rapid comparison between all phases.

The Gibbs free energy associated with the $F^- = OH^-$ substitution per site and normalised to phlogopite (Fig. 5A) ranges from ~ -13 $kJ.mol^{-1}$ for the $OH4^{Prg}$ of pargasite to more than 60 $kJ.mol^{-1}$ in pistacite and several sites of chlorite and carpholite end-members. Sites of aspidolite and pargasite - with the exception of $OH2^{Prg}$ - display negative values lower than -1 $kJ.mol^{-1}$, the lowest being for $OH4^{Prg}$ (-13 $kJ.mol^{-1}$). Independent sites in a single mineral may display large energy differences. This spread is limited in micas (≤ 10 $kJ.mol^{-1}$), larger in pargasite, kaolinite and lizardite (~ 20 $kJ.mol^{-1}$) and very large for clinochlore (more than 40 $kJ.mol^{-1}$ between sites of the T-O-T sheet and of the brucite-like sheet) and carpholite (around 40 $kJ.mol^{-1}$ between the two sites). The energy difference is also important in sudoite, but the T-O-T sites are not

substantially favoured as in clinochlore. There is a strong difference between dioctahedral and trioctahedral phyllosilicates. Trioctahedral layers show lower defect energies than the dioctahedral ones. Differences between K- and Na-bearing micas are small, but larger in biotite than in white micas. For the amphibole group, the sites of pargasite are systematically preferred to those of tremolite. In epidote, incorporation of F is very costly, with clinozoisite slightly favoured over pistacite. Carpholite and Mg-carpholite yield comparable results, with their OH1 site strongly favoured over OH2.

Figure 5B shows the computations for the $Cl^- = OH^-$ exchange. The general trends described above for F are also observed. However, energy differences between sites in a single phase appear globally larger for Cl and Br than for F. There is a ~ 250 kJ.mol^{-1} gap between the most ($OH4^{Prg}$) and the least ($OH1^{Czo}$) favourable sites for Cl uptake. Trioctahedral phyllosilicates globally show lower defect energies than dioctahedral ones, but this is less clear-cut than for the $F^- = OH^-$ exchange, especially for clinochlore and sudoite. Incorporation of Cl in $OH4^{Asp}$, $OH3^{Asp}$, $OH4^{Prg}$ and $OH2^{Prg}$ is favoured over $OH1^{Phl}$. Pargasite shows the lowest defect energy for Cl incorporation, as for F. Interestingly, clinozoisite shows higher defect energy than pistacite for Cl uptake, in opposite direction to F.

Figure 5C displays the results for the $Br^- = OH^-$ exchange. The difference between the most ($OH4^{Prg}$) and the least ($OH1^{Czo}$) favourable sites is larger than for the two other exchanges, reaching ~ 300 kJ.mol^{-1}, and energetic differences between independent sites are also larger than for Cl and F. The previously observed gap between trioctahedral and dioctahedral phyllosilicates is not clear, with sites of sudoite and kaolinite having lower defect energies than $OH1^{Tlc}$ and similar to that of $OH4^{Phl}$. $OH2^{Lz}$ is also slightly favoured over $OH1^{Phl}$. Differences between defect energies of phlogopite sites amount to ~ 20 kJ.mol^{-1} for Br uptake, ten times larger than for F. For clinochlore, the gap between the T-O-T sheet and the brucite-like sheet is smaller than for the $Cl^- = OH^-$ and $F^- = OH^-$ exchanges (~ 20 kJ.mol^{-1} here against 40 kJ.mol^{-1} for Cl and F uptake).

In summary, these results show that the energetic cost of the incorporation of halogens depends on the mineral structure, on the mineral composition and on the site of incorporation. Trends and differences between sites and between crystals holding for F are not necessarily observed for heavier halogens.

Crystal chemical controls over halogen distribution

The role of steric hindrance

Steric hindrance is an obvious control on halogen uptake, due to the size difference between OH and halogen species. As expected, computations indicate that strain globally increases with halogen size. The importance of steric hindrance for Cl and Br uptake is clear (Fig. 3-4), as shown by the deviation of Cl and Br from the original OH site. Strain is accommodated by the direct environment of the defect site, including deformation and tilting of tetrahedral and octahedral sites. This strain dependency on halogen size is observed in all minerals modelled here, and strain patterns reflect incorporation of defect cations (see e.g. Juhin et al. 2008; Angel et al. 2012; Figowy et al. 2020).

Steric hindrance amounts to energetic cost, as shown in Fig. 5. As an example, Br incorporation is similarly easy in the large cage-like OH1 site of carpholite as in the OH sites of phlogopite. In contrast, the energetic cost of halogen incorporation in epidote is very high and increases strongly with steric hindrance, consequently epidote does not accommodate any halogen easily in its OH site.

Halogens in phyllosilicates

The phyllosilicate group includes well-known halogen-bearing minerals such as phlogopite. Figure 5 highlights that halogen incorporation is not driven solely by steric hindrance (see the evolution of defect energies). Phyllosilicates share comparable structures, but defect energies are very different, even for the same halogen. This section aims at disentangling competing effects of structure and composition of the host mineral and of hosted halogen over their incorporation.

Effect of octahedral vacancies

An important difference between phyllosilicates is the occupancy of the octahedral layer, which induces a difference in OH orientation (see “Optimised structures” above). The occupancy of the octahedral sheet exerts a strong control on F uptake in T-O, T-O-T and T-O-T-O phyllosilicates, independently from the interlayer charge. Trioctahedral layers of phyllosilicates are systematically favoured over dioctahedral layers for F incorporation (Fig. 5A). F favours muscovite/paragonite for dioctahedral phyllosilicates and phlogopite/aspidolite for trioctahedral phyllosilicates.

The Online Resources 3 and 4 are used to compare the geometry of OH groups and their neighbouring tetrahedra in phyllosilicates studied here to the compilation by Ceccarelli et al. (1981) who reported the neutron geometry of non-linear hydrogen bonded systems (see also Nyfeler and Armbruster (1998) for hydrogen bonds in silicates). The difference of orientation of the OH group in dioctahedral and trioctahedral phyllosilicates supports stronger hydrogen interactions in dioctahedral phyllosilicates than in trioctahedral ones.

The role of the octahedral sheet occupancy over F uptake has been discussed by several authors who also considered hydrogen interactions (Robert and Kodama 1988; Robert et al. 1993). In dioctahedral phyllosilicates, the local charge deficiency due to the vacancy causes polarisation of the OH group, with hydrogen bonding between the hydroxyl and the nearest tetrahedron (towards which the OH group is pointing, compare Fig. 2A and 2B). In trioctahedral phyllosilicates, the OH group is rather acting as a point charge without hydrogen bonding with the neighbouring tetrahedron. The hydrogen bond in dioctahedral phyllosilicates increases the energetic cost of F substitution. The energy difference (Fig. 5) between di- and trioctahedral phyllosilicates clearly supports this point and helps quantifying this effect.

Effect of tetrahedral occupancy and Si/Al ordering

The influence of Si = Al substitution on F incorporation in dioctahedral and trioctahedral micas has been discussed by Robert et al. (1993). They proposed that the distribution of Si and Al in tetrahedra around the OH site creates local heterogeneities of charges, influencing the strength of hydrogen bonds between OH and the tetrahedra. In agreement, Figure 5 shows that the Si-Al distribution has an influence on halogen uptake. Results for phlogopite, aspidolite, muscovite and paragonite display small energetic differences between the independent OH sites for the same phase. The only difference between these sites is the occupancy of the surrounding tetrahedra, either by Al or Si.

The tetrahedral occupancy does not seem to influence F incorporation in phlogopite, where the defect energy of the four OH sites are very similar. This is not so in muscovite and paragonite where the OH4 site (surrounded by two Al and four Si) is favoured.

For Cl and Br uptake, steric hindrance overprints the effect of the tetrahedral site occupancy. Cl and Br behave similarly in each mica and appear equivalently influenced by tetrahedral occupancy changes. The distribution of Si and Al in tetrahedra influences Cl and Br uptake in phlogopite to a small extent, OH4 being less favourable for both. In dioctahedral micas, the OH3 site (only surrounded by Si atoms) is also systematically less favourable. Interestingly, the opposite behaviour is observed in aspidolite, where the incorporation of Cl and Br is favoured when tetrahedra are only occupied by Si. This suggests that the control of Si/Al distribution on halogen uptake in these phases is complex in that composition and structural changes have cumulative and competing effects.

Overall, the effect of tetrahedral occupancy appears limited in comparison with that of the composition of octahedral sites and steric hindrance caused by the halogen, which are larger in magnitude.

Electrostatic interactions with alkalis

The presence and nature of interlayer alkalis have been shown to be important for halogen uptake in phyllosilicates (e.g. Robert et al. 1993). It is intimately linked to the orientation of OH groups. Halogens are predicted to favour trioctahedral over dioctahedral mica (Fig. 5). This is partly explained by electrostatic interactions between OH and the alkali in the interlayer space. In trioctahedral mica, the OH group is almost pointing towards the alkali, inducing a H^+-K^+ or H^+-Na^+ repulsion. This effect is much weaker in dioctahedral mica due to the higher distance between OH and the alkali. During the halogen = OH substitution, the repulsive interaction in trioctahedral mica is replaced by attraction between the alkali and the halogen, making halogen uptake very favourable in these structures. This stabilization is limited in dioctahedral mica, where halogen incorporation is also made difficult due to vacancies (see "Effect of octahedral vacancies" above). The effects of hydrogen bonding in the T-O-T layer and of interaction with interlayer alkali are cumulative in mica, both related to the OH orientation. This point has also been described experimentally by Robert et al. (1993) in potassic mica.

The effect of the nature of the alkali cation has been tested by comparing results on potassic and sodic micas. K^+ and Na^+ ions have the same charge but differ by their ionic radius, of 1.39 Å for Na^+ against 1.64 Å for K^+. Defect energy computations of phlogopite and aspidolite display quantifiable differences (~ 15 kJ.mol^{-1} for F incorporation into $OH1^{Phl}$ and $OH1^{Asp}$, Fig.5A), attesting to the role of the interlayer space composition. These differences are small but larger than those induced by Si/Al ordering.

The small difference may be explained by steric hindrance: for example, the incorporation of Cl and Br in the OH4 site of dioctahedral micas induces a small increase of the volume of the neighbouring alkali site, respectively of ~ +1 % vol. and +1.6 % vol. in

muscovite, against +2.5 % vol. and +2.8 % vol. in paragonite. The K-O distances also follow this trend, most of them being slightly stretched after Cl or Br incorporation. The site volume increase is easier near the larger K^+ ion than near Na^+, promoting incorporation of heavier halogens in muscovite. In paragonite, the interlayer site undergoes a slightly larger dilatation after Cl and Br incorporation than the interlayer site of muscovite, which may decrease the ionic bond strength between the alkali and the anions of the sheets. In the case of F, the volume of the alkali site displays a small contraction, of -0.4 % in muscovite and -0.5 % in paragonite. This tends to favour paragonite. The example suggests that the incorporation of halogens at trace amounts – especially Cl and Br – may depend on the Na/K ratio in micas.

Halogens in amphibole

Effect of tetrahedral and octahedral occupancy

When incorporating F, Cl or Br in pargasite, there are clearly differences between OH sites in terms of defect energies. These differences may be related to the Si/Al distribution in tetrahedra. The absence of tetrahedral Al in the neighbourhood of OH3 does not seem to impact F and Cl uptake, but in the case of Br, OH3 is the least favoured site for substitution. The OH4 site, which is favoured over all sites of pargasite for all halogens, is surrounded by four Si and two Al atoms. The gap between the four sites of pargasite is globally larger than in mica, suggesting that the effect of Si/Al distribution is greater in amphibole than in mica.

Electrostatic interactions with alkalis and alkaline earths

As for mica, electrostatic attraction between halogens and alkalis appears important in amphibole. Tremolite and pargasite contain Ca in their structure. In addition, Na occupies the A-site of pargasite. The OH groups in amphiboles are generally pointing towards the Na^+ cation, the hydrogen atom being ~ 3 Å from the alkali. The incorporation of halogen suppresses the H^+-Na^+ repulsion and replaces it by attraction between Na and the halogen anion. This provides an explanation as to why pargasite has lower defect energies than tremolite, which does not contain Na. The energy difference between pargasite and tremolite decreases with the radius of the incorporated halogen due to steric hindrance. Ca is found in both amphiboles; however, the OH sites are far from Ca (more than 5 Å) and not oriented towards it. This suggests that its role in halogen incorporation is negligible compared to that of Na.

Halogens in carpholite

Local electrostatic interactions

The two sites of carpholite show large differences in defect energies (Fig. 5A). In the case of F, the difference may be explained by electrostatic interactions. The OH1 site is adjacent to one Al and one Mn or Mg, whereas the OH2 site is adjacent to two Al and one Mn or Mg. Substitution of OH1 by F requires breaking two bonds contrary to the case of OH2, which may promote the incorporation of F into the former site. In addition, Fuchs et al. (2001) showed that the OH2 site of Mg-carpholite forms hydrogen bonds with surrounding oxygen atoms, unlike OH1. As in micas, the presence of hydrogen bonds may disadvantage even more the F = OH2 substitution. All these parameters are probably at play for Cl and Br incorporation, and superimposed to steric hindrance, leading to huge energetic differences between the two sites.

The role of octahedral occupancy

The main difference between carpholite and its Mg-equivalent is octahedral occupancy. Focusing on the OH1 site (which has the lowest defect energy), the difference in defect energies is ~ 5 $kJ.mol^{-1}$ for F and 10 $kJ.mol^{-1}$ for Cl and Br. F is more favourably hosted in Mg-carpholite, Cl and Br in carpholite. This is explained as for mica: the OH1 site of carpholite is more strained than that of Mg-carpholite, promoting Cl and Br incorporation in carpholite. These results show that the incorporation of halogens in carpholite may slightly depend on the Mg/Mn ratio of the mineral.

The role of octahedral occupancy in epidotes

Clinozoisite and pistacite are computed as very unfavourable hosts for halogen incorporation, with large defect energies (Fig. 5) and clinozoisite showing the highest defect energies for Cl and Br. Differences between the two probably arise from the nature of the octahedral cation, although the difference in energetic cost is remarkably large, especially in the case of Cl and Br. This is explained by the high sensitivity of epidote to steric hindrance, in structures where halogens are globally unwelcome.

Cl and Br are behaving similarly, with pistacite being a less unfavourable host. F prefers clinozoisite. This points to easier incorporation near Fe^{3+} sites (r_{Fe3+} = 0.645 Å), slightly larger than Al sites (r_{Al3+} = 0.535 Å), and therefore more prone to deformation. Differences appear small but comparison may be made with garnet: Dubacq and Plunder (2018) have shown that limited increase of the octahedral site of pyrope by incorporation of a few percent of grossular component leads to increasing Sr partitioning by orders of magnitude. It remains that clinozoisite and pistacite are unlikely halogen hosts.

Halogen partitioning

The set of minerals used above allows evaluating the partitioning of halogens into mineral assemblages representative of subduction zone metamorphic grades. These assemblages remain simplistic as they are restricted to end-member compositions and do not include iron-bearing minerals, but allow first-order observations with vast implications.

Halogen partitioning between sites

Defect energies and Gibbs energies of reactions are translated into partition coefficients, crystal site per crystal site, with Eq. 4. For phases with several OH sites, exchange reactions are written between the sites of the mineral and between minerals. This is equivalent to reciprocal solid solutions.

Table 2 displays partition coefficients between the OH1 site of each selected mineral and the other independent sites. A value above 1 shows that the OH1 site of the mineral is favoured for halogen incorporation. The partition coefficients between sites of a same mineral – at a given temperature – may differ by orders of magnitude, due to the combination of crystal chemical effects described above, depending on the mineral and on the incorporated halogen.

In potassic mica, the difference between OH sites is limited compared with the other minerals of Table 2. The OH sites of phlogopite are almost equivalent for F uptake, but the OH4 site is clearly disadvantaged in the case of Cl ($K^{Phl}_{OH1/OH4}$ = 7.3) and Br ($K^{Phl}_{OH1/OH4}$ = 18). OH sites of muscovite appear globally more heterogeneous, $OH1^{Ms}$ and $OH4^{Ms}$ being clearly favoured over $OH2^{Ms}$ and $OH3^{Ms}$, especially for Cl and Br uptake. In lizardite, the affinity of halogens for $OH2^{Lz}$ – between Si-filled tetrahedra – translates as almost all of Cl being distributed in $OH2^{Lz}$ rather than $OH1^{Lz}$, with a partition coefficient of $5.2.10^{-4}$. To a lesser extent, this is also the case in kaolinite for F and Cl incorporation.

In pargasite, partition coefficients indicate large differences between OH sites even in the case of F, with a value of 4.1 for the $OH1^{Prg}$-$OH2^{Prg}$ exchange, in favour of $OH1^{Prg}$. The strongest differences in partition coefficients are computed for the Cl = OH substitution, where $OH1^{Prg}$ is clearly disadvantaged, reaching up to 10^{-3}. In Mg-carpholite, the difference between OH sites is spectacular. The case of clinochlore highlights the differences between incorporation in the T-O-T layer or in the gibbsite-like layer. The $OH1^{Clc}$, $OH2^{Clc}$ and $OH3^{Clc}$ sites of the T-O-T layer are systematically very favoured by halogens, with a gap of more than two orders of magnitude compared to the OH sites of the brucite-like layer. The largest partition coefficients are computed for Cl, up to almost 10^6 in favour of $OH1^{Clc}$.

These highly variable partition coefficients underline the importance of assessing the respective contribution of each site to calculate a partition coefficient between minerals – far away from averaging site-by-site partition coefficients.

The partition coefficient for halogen exchange between minerals with several sites is obtained through summation of individual (site-by-site) partition coefficients. This is exemplified for partitioning between phlogopite and pargasite (reaction R4) which have four independent OH sites in the supercells.

$$\text{F-Prg} + \text{Phl} = \text{F-Phl} + \text{Prg} \qquad \text{(R4)}$$

The molar partition coefficient $D_F^{Phl/Prg}$ is defined as the ratio between n_F^{Phl} the number of moles of F in phlogopite and n_F^{Prg} that of pargasite (Eq. 5, see also Morse, 2015, for definitions). n_F^{Phl} is the sum of moles of F in each OH site of phlogopite, with occupation statistics calculated from defect energies with site-by-site partition coefficients (Eqs. 1-4), multiplied by the multiplicity m_i of each i site (Eq. 5). n_F^{Prg} is computed similarly over j sites in the following:

$$D_{\mathrm{F}}^{\mathrm{Phl/Prg}} = \frac{n_{\mathrm{F}}^{\mathrm{Phl}}}{n_{\mathrm{F}}^{\mathrm{Prg}}} = \frac{\sum_{(i)} m_i . n\mathrm{OH}i^{\mathrm{Phl}}}{\sum_{(j)} m_j . n\mathrm{OH}j^{\mathrm{Prg}}}. \qquad (5)$$

Mass partition coefficients are obtained from their molar equivalents after multiplication by the ratio of masses. It is noteworthy that this correction is important as the mass ratio may differ from 1 depending on the composition and selected anionic basis (~ 0.5 for that of $O_{10}(OH)_2$ phlogopite and $O_{22}(OH)_2$ pargasite).

Halogen partitioning between hydrous silicates

The partitioning of halogens has been estimated for three representative mineral assemblages of distinct

metamorphic grades in Fig. 6: pargasite – phlogopite – clinozoisite (ca. 700° C, granulitic facies), tremolite – muscovite – paragonite (ca. 500° C, greenschist facies) and clinochlore – pyrophyllite – Mg-carpholite – muscovite (ca. 400° C, low-temperature blueschist facies). Corresponding exchange reactions and associated mass partition coefficients are indicated in Fig. 6 for each halogen. In Table 3, three assemblages are added for medium to low temperature conditions: clinochlore – phlogopite – muscovite (ca. 500° C, low-grade metamorphism), talc – lizardite (ca. 300° C) and lizardite – kaolinite (ca. 200 °C). These assemblages allow identifying the main hosts for F, Cl and Br at different metamorphic grades. Comparison to partition coefficients derived from experiments or natural samples is favourable but remains qualitative for four reasons: i) data are sparse, ii) calculations are carried out for end-members and the effect of solid solutions such as Tschermak exchange in chlorite, mica and amphibole cannot be estimated straightforwardly, iii) natural and experimental assemblages may contain halogens in concentrations above the dilute limit, where partition coefficients become concentration-dependent, iv) Fe^{2+} could not be included in the simulations. All these points are opportunities for future research.

Varying mineral assemblages with metamorphic conditions

The pargasite – phlogopite – clinozoisite assemblage (Fig. 6A) indicates that F partitions slightly in favour of pargasite, with a mass partition coefficient of 1.4 between both minerals. Cl and Br displays respective $D^{Prg/Phl}$ partition coefficients of ~ 21 and 18 in favour of the amphibole, showing pargasite is favoured over phlogopite. Clinozoisite shows very low partition coefficients for Cl and Br, showing that essentially it does not incorporate any halogen in this assemblage. Ekström (1972) measured F partition coefficients ranging from 0.5 to 1.1 between calcic amphibole and biotite from metamorphic iron ores in Sweden (at temperatures of ~ 530° C). The partition coefficient for F estimated here of ~ 1.4 between pargasite and phlogopite appears realistic, considering uncertainties associated with temperature estimations and with the composition dependency.

All three halogens show systematic preference for tremolite when equilibrated with muscovite and paragonite (Fig. 6B), more so for heavy halogens than for F ($D_F^{Tr/Ms}$ = 73 and $D_F^{Tr/Pg}$ = 50 in favour of tremolite). The small differences in partition coefficients between paragonite and muscovite reflect the effect of the interlayer cation.

The lower grade clinochlore – pyrophyllite – muscovite – Mg-carpholite assemblage (Fig. 6C) shows that clinochlore is the favoured host for all three halogens. The computed partition coefficient indicates that F is almost equally distributed between clinochlore and Mg-carpholite, whereas partitioning of heavier halogens is more strongly in favour of clinochlore ($D_{Cl}^{Car/Clc}$ = 0.2 and $D_{Br}^{Car/Clc}$ = 0.3). Dioctahedral phyllosilicates (muscovite and pyrophyllite) are clearly less attractive to halogens.

In the clinochlore – phlogopite – muscovite assemblage (Table 3), phlogopite is favoured over the other two minerals. F and Br appear more likely hosted by clinochlore. Cl partitions preferentially into biotite, but smaller quantities may be stored into clinochlore ($D_{Cl}^{Phl/Clc}$ = 36). Again the dioctahedral phyllosilicate (here muscovite) is clearly disadvantaged. Evans (1969) measured F and Cl amount in coexisting muscovite and biotite in high-temperature metamorphic conditions (along the sillimanite – orthoclase isograde). The corresponding partition coefficient is ~ 5 in favour of the trioctahedral mica. Munoz and Ludington (1977) determined experimentally a constant of reaction of ~ 40 for the $F^- = OH^-$ exchange between phlogopite and muscovite (in favour of phlogopite), independently of temperature. Our calculations also indicate phlogopite as the favoured phase, but with a larger $D_F^{Phl/Ms}$ partition coefficient (see Table 3). This difference may originate from the composition of the natural samples of Evans (1969) with significant iron content, especially in biotite (average XMg of biotite ~ 40, against XMg above 50 for muscovite), as high Mg/Fe ratio is known to ease F incorporation in micas (e.g. Ramberg 1952; Volfinger et al. 1985). According to Teiber et al. (2015) who measured ~ 105 ppm Br in biotite, it is also able to store Br in subduction zones.

In the low-temperature lizardite – talc assemblage (Table 3), Cl and Br are stored in serpentine but almost not in talc. F partitions more favourably into lizardite, but the relatively small partition coefficient (D_F^{Lz-Tlc} = 16) suggests that some F may be found in talc. The role of serpentine in hosting halogens has been demonstrated by several studies (e.g. John et al. 2011; Bernini et al. 2013; Pagé et al. 2018). Pagé et al. (2018) measured the concentrations of F, Cl, Br and I in serpentine and underlined their crucial role in transporting halogens in subduction zones.

In the near-surface lizardite – kaolinite assemblage (Table 3), all three halogens are clearly incorporated into lizardite. Interestingly, the partition coefficient is much smaller for Br than for Cl and F, reflecting differences in steric hindrance between trioctahedral and dioctahedral phyllosilicates. As a consequence, in the context of alteration, kaolinite may store small amounts of Br.

To summarize briefly, pargasitic amphibole, biotite and lizardite appear as important hosts for all halogens, in agreement with previous studies. Clinochlore also appears as a likely host for the three halogens to a lesser extent. Carpholite and tremolite seem to store some halogens at low-grade metamorphism conditions, especially in the case of F. Talc may incorporate some F but no heavier halogens if serpentine, biotite or pargasite are present. Generally, dioctahedral phyllosilicates and epidote appear poor hosts for halogens, regardless of temperature. Dioctahedral mica is an exception as it may store F, especially in the absence of trioctahedral phyllosilicates (e.g. Evans 1969; Munoz and Ludington 1977).

Fractionation of halogens during subduction

The partition coefficients given above reflect the predicted distribution of small amount of halogens in predefined mineral assemblages, absolute values are not accessed and cannot be assessed with this method. Yet it is noteworthy that the equilibrium modelling shown here with increasing metamorphic grade predicts fractionation of halogens (in the sense of modification of the F/Cl/Br ratios of assemblages) among minerals due to steric hindrance and electrostatic effects, especially between F and heavier halogens. This implies deviation from original F/Cl/Br ratios of fluids at equilibrium with evolving mineral assemblages, and fluid expulsion will show evolving halogen ratios. Overall, F is predicted to be more homogeneously distributed among silicates than heavier halogens, as several hydrous silicates may act as minor carriers of F, such as Mg-carpholite and talc. In addition, increasing metamorphic grade, leading to crystallization of amphibole, will affect F much less than Br and Cl which will partition into amphibole even in the presence of biotite.

These results are consistent with previous work on the geochemical cycle of halogens in subduction, which described strong differences between the geochemical behaviour of F and that of Cl, Br and I. Due to their incompatible behaviour, most of the heavy halogens are sent back to the surface via arc volcanism processes (e.g. Ito et al. 1983; Spandler and Pirard 2013; Zellmer et al. 2015; Hecker et al. 2020; Louvel et al. 2020). Subducted Cl may also be partly kept in the slab and transported deeper in the mantle (see John et al. 2011; Barnes et al. 2019). In contrast, most of the subducted F is trapped in the slab, in mica, amphibole and serpentine (Luth 2003; Spandler et Pirard 2013; Zellmer et al. 2015; Hecker et al. 2020; Louvel et al. 2020). Pagé et al. (2017) estimated that ~ 95 % of subducted F was not recycled at the surface. This is consistent with the greater compatibility of F in hydrous silicates calculated here, and with the restricted number of minerals effectively incorporating Cl and Br: amphibole destabilization will have stronger effect on heavier halogens.

The overruling effect of steric hindrance over Br also suggests fractionation between Cl and Br during prograde metamorphism, although on a smaller scale than between F and heavier halogens. The storage of Cl in hydrous silicates is estimated as much easier in pargasite and biotite at high temperature, and in lizardite, carpholite and tremolite at lower metamorphic grade. In these assemblages, Br appears slightly more enriched in kaolinite and chlorite, but in all minerals tested here Br is hard to incorporate due to steric hindrance, whereas electrostatic interactions have relatively larger competing effects for Cl. This translates into varying distribution of Br and Cl during metamorphism reactions, and higher affinity of Br for fluids.

Conclusions and perspectives

This work uses first-principles computations to investigate the importance of crystal chemical parameters on F, Cl and Br incorporation in hydrous silicates, and provides a framework with worked examples to estimate partition coefficients for halogens at trace amounts.

Distances between defects above ~ 10 Å allow reproducing trace behaviour (for Cl and Br, this value being at least 9 Å for F). This is a measure of the strain field around halogen-bearing defects, above which strain computed at cell scale becomes negligible.

Steric hindrance and electrostatic interactions between ions are major controls over halogen distribution between minerals. The incorporation of F, Cl or Br appears highly dependent on octahedral site occupancy in all minerals modelled here. In amphibole and mica, the alkali content is also an important parameter due to attractive interactions with halogens. The distribution of Si and Al in tetrahedral sites may also influence halogen uptake to a lesser extent, by disturbing the charge repartition in the host mineral, in turn modifying the electrostatic behaviour of OH groups. The importance of steric hindrance is dominant for heavy halogens.

Estimated partition coefficients in representative mineral assemblages in the $KNaCaMnMFe^{3+}ASH$ system give pargasitic amphibole, biotite and lizardite as likely hosts for halogens in subduction zones, consistently with previous work. Pargasite appears as the most favourable hydrous silicate for Cl and Br storage. Clinochlore, tremolite and carpholite come second. Dioctahedral phyllosilicates and epidote are generally unlikely to store halogens with the exception of F in muscovite.

This modelling provides evidence for fractionation between F and heavier halogens, consistently with geochemistry and volcanology studies. Differences in partition coefficients are also observed between Cl and Br, but on a smaller scale than for F. At subduction zone scale, this is consistent with the similar behaviour of Cl and Br.

Comparison of calculated partition coefficients with literature values is favourable but remains qualitative, offering research perspectives, among which modelling of Fe^{2+}-rich minerals is important as studies have highlighted the role of Fe^{2+} on F and Cl uptake in mica (e.g. Ramberg 1952; Volfinger et al. 1985; Morrison 1991; Boukili et al. 2002; Chevychelov et al. 2008). In addition, the potential role of minor or trace elements (e.g. Li, Be, B, REE) on halogen incorporation, possibly through joined incorporation with halogens, could be quantified using the method described here.

Future research efforts should include modelling of iodine to better understand its incorporation in silicates, as measurements remain very sparse (see e.g. the work of Pagé et al. (2018) on serpentines) and the partitioning of iodine between mica, serpentine, and/or amphibole is unknown.

Eventually, addition of other minerals to the dataset presented here will allow more realistic modelling of halogen partitioning into subduction-zone rocks. This includes lawsonite, an important carrier of volatiles (see e.g. Cook-Kollars et al. 2014; Lefeuvre et al. 2020) which was not modelled here due to its molecular water content, and anhydrous silicates where halogens are incorporated via coupled substitutions such as in sphene: $Ti^{4+} + O^{2-} = F^{-} + Al^{3+}$.

References

Agard P, Labrousse L, Elvevold S, Lepvrier C (2005) Discovery of Paleozoic Fe-Mg carpholite in Motalafjella, Svalbard Caledonides: a milestone for subduction-zone gradients. Geology 33(10):761-764. https://doi.org/10.1130/G21693.1

Allan NL, Du Z, Lavrentiev MY, Blundy JD, Purton JA, van Westrenen W (2003) Atomistic simulation of mineral–melt trace-element partitioning. Phys Earth Planet Inter 139(1-2):93-111. https://doi.org/10.1016/S0031-9201(03)00147-X

Allègre CJ, Treuil M, Minster JF, Minster B, Albarède F (1977) Systematic use of trace element in igneous process. Contrib to Mineral Petrol 60(1):57-75. https://doi.org/10.1007/BF00372851

Angel RJ, Sochalski-Kolbus LM, Tribaudino M (2012) Tilts and tetrahedra: the origin of the anisotropy of feldspars. Am Mineral, 97(5-6):765-778. https://doi.org/10.2138/am.2012.4011

Angiboust S, Agard P (2010) Initial water budget: The key to detaching large volumes of eclogitized oceanic crust along the subduction channel? Lithos 120(3-4):453-474. https://doi.org/10.1016/j.lithos.2010.09.007

Aprà E, Causa M, Prencipe M, Dovesi R, Saunders VR (1993) On the structural properties of NaCl. An *ab initio* study of the B1-B2 phase transition. J Phys Condens Matter 5:2969-2976.

Aranovich L, Safonov O (2018) Halogens in high-grade metamorphism. In: Harlov DE, Aranovich L (eds) The role of halogens in terrestrial and extraterrestrial geochemical processes: surface, crust, and mantle. Springer, Berlin, pp 713–757. http://link.springer.com/10.1007/978-3-319-61667-4_11

Banno Y, Miyawaki R, Kogure T, Matsubara S, Kamiya T, Yamada S (2005) Aspidolite, the Na analogue of phlogopite, from Kasuga-mura, Gifu Prefecture, central Japan: description and structural data. Mineral Mag 69(6):1047-1057. https://doi.org/10.1180/0026461056960307

Barnes, JD, Penniston-Dorland SC, Bebout GE, Hoover W, Beaudoin GM, Agard P (2019) Chlorine and lithium behavior in metasedimentary rocks during prograde metamorphism: a comparative study of exhumed subduction complexes (Catalina Schist and Schistes Lustrés). Lithos 336-337:40-53. https://doi.org/10.1016/j.lithos.2019.03.028

Bernini D, Wiedenbeck M, Dolejš D, Keppler H (2013) Partitioning of halogens between mantle minerals and aqueous fluids: implications for the fluid flow regime in subduction zones. Contrib to Mineral Petrol 165(1):117-128. https://doi.org/10.1007/s00410-012-0799-4

Bish DL (1993). Rietveld refinement of the kaolinite structure at 1.5 K. Clays Clay Miner 41(6):738-744. https://doi.org/10.1346/CCMN.1993.0410613

Bookin AS, Drits VA (1982). Factors affecting orientation of OH-vectors in micas. Clays Clay Miner 30(6):415-421. https://doi.org/10.1346/CCMN.1982.0300603

Boukili B, Holtz F, Bény JM (2002) Fe-F and Al-F avoidance rule in ferrous-aluminous (OH, F) biotites. Schweiz Mineral Petrog Mitt 82 :549-559. https://doi.org/10.5169/seals-62380

Carpenter MA, McKnight REA, Howard CJ, Zhou Q, Kennedy BJ, Knight KS (2009) Characteristic length scale for strain fields around impurity cations in perovskites. Phys Rev B 80(21):214101. https://doi.org/10.1103/PhysRevB.80.214101

Catti M, Ferraris G, Ivaldi G (1989) Thermal strain analysis in the crystal structure of muscovite at 700 °C. Eur J Mineral 1:625-632. https://doi.org/10.1127/ejm/1/5/0625

Catti M, Valerio G, Dovesi R, Causà M (1994) Quantum-mechanical calculations of the solid-state

equilibrium MgO + alpha-Al_2O_3 = $MgAl_2O_4$ (spinel) versus pressure. Phys Rev B 49: 14179-14187. https://doi.org/10.1103/PhysRevB.49.14179

Catti M, Valerio G, Dovesi R (1995) Theoretical study of electronic, magnetic, and structural properties of alpha-Fe_2O_3 (hematite). Phys Rev B 51: 7441-7450. https://doi.org/10.1103/PhysRevB.51.7441

Ceccarelli C, Jeffrey GA, Taylor R (1981) A survey of OH···O hydrogen bond geometries determined by neutron diffraction. J Mol Struct 70:255-271. https://doi.org/10.1016/0022-2860(81)80112-3

Chevychelov VY, Botcharnikov RE, Holtz F (2008) Experimental study of fluorine and chlorine contents in mica (biotite) and their partitioning between mica, phonolite melt, and fluid. Geochemistry Int 46(11):1081-1089. https://doi.org/10.1134/S0016702908110025

Civalleri B, Ferrari AM, Llunell M, Orlando R, Merawa M, Ugliengo P (2003) Cation selectivity in alkali-exchanged chabazite: an *ab initio* periodic study. Chem Mater 15: 3996-4004. https://doi.org/10.1021/cm0342804

Cook-Kollars J, Bebout GE, Collins NC, Angiboust S, Agard P (2014) Subduction zone metamorphic pathway for deep carbon cycling: I. Evidence from HP/UHP metasedimentary rocks, Italian Alps. Chem Geol 386:31-48. https://doi.org/10.1016/j.chemgeo.2014.07.013

Daigle NM (2015) Chlorine enrichment of hydrous minerals in Archean granulite facies ironstone from the Beartooth Mountains, Montana, USA: Implications for high-grade metamorphic fluids. Master's Theses, Louisiana State University, 1188. https://digitalcommons.lsu.edu/gradschool_theses/1188

D'Arco P, Sandrone G, Dovesi R, Orlando R, Saunders VR (1993) A quantum mechanical study of the perovskite structure type of $MgSiO_3$. Phys Chem Miner 20:407-414. https://doi.org/10.1007/BF00203110

De La Pierre M, Demichelis R, Dovesi R (2016) Vibrational spectroscopy of minerals through *ab initio* methods. In: Kubicki JD (ed) Molecular modeling of geochemical reactions: an introduction. John Wiley and Sons, UK, pp 341-374.

Dollase WA (1968) Refinement and comparison of the structures of zoisite and clinozoisite. Am Mineral 53(11-12):1882-1898.

Dove MT, Thayaparam S, Heine V, Hammonds KD (1996) The phenomenon of low Al-Si ordering temperatures in aluminosilicate framework structures. Am Mineral 81(3-4):349-362. https://doi.org/10.2138/am-1996-3-409

Dovesi R, Ermondi E, Ferrero E, Pisani C, Roetti C (1983) Hartree-Fock study of lithium hydride with the use of a polarizable basis set. Phys Rev B 29:3591-3600. https://doi.org/10.1103/PhysRevB.29.3591

Dovesi R, Roetti C, Freyria Fava C, Prencipe M, Saunders VR (1991) On the elastic properties of lithium and potassium oxide. An *ab initio* study. Chem Phys 156:11-19. https://doi.org/10.1016/0301-0104(91)87032-Q

Dovesi R, Orlando R, Civalleri B, Roetti C, Saunders VR., Zicovich-Wilson C (2005) CRYSTAL: A computational tool for the ab initio study of the electronic properties of crystals. Z Kristallogr Cryst Mater 220(5-6):571-573. https://doi.org/10.1524/zkri.220.5.571.65065

Dovesi R, Orlando R, Erba A, Zicovich-Wilson MC, Civalleri B, Casassa SM, Maschio L, Ferrabone M, De La Pierre M, D'Arco P, Noel Y, Causà M, Rérat M, Kirtman B (2014) CRYSTAL14: a program for the *ab initio* investigation of crystalline solids. Int J Quantum Chem 114:1287-1317. https://doi.org/10.1002/qua.24658

Dubacq B, Plunder A (2018) Controls on trace element distribution in oxides and silicates. J Petrol 59(2):233-256. https://doi.org/10.1093/petrology/egy027

Eggleton RA, Bailey SW (1967) Structural aspects of dioctahedral chlorite. Am Mineral 52(5–6):673–689

Ekström TK (1972) The distribution of fluorine among some coexisting minerals. Contr Mineral Petrol 34(3):192-200. https://doi.org/10.1007/BF00373291

Evans BW (1969) Chlorine and fluorine in micas of pelitic schists from the sillimanite-orthoclase isograd, Maine. Am Mineral 54(7-8):1209-1211.

Figowy S, Dubacq B, Noël Y, D'Arco P (2020) Partitioning of chromium between garnet and clinopyroxene: First-principle modelling versus metamorphic assemblages. Eur J Mineral 32(4):387-403. https://doi.org/10.5194/ejm-32-387-2020

Fuchs Y, Mellini M, Memmi I (2001) Crystal-chemistry of magnesiocarpholite: controversial X-ray diffraction, Mossbauer, FTIR and Raman results. Eur J Mineral 13(3):533-543. https://doi.org/10.1127/0935-1221/2001/0013-0533

Galvez ME, Connolly JAD, Manning CE (2016) Implications for metal and volatile cycles from the pH of subduction zone fluids. Nature, 539(7629):420-424. https://doi.org/10.1038/nature20103

Giese RF (1975) The effect of F/OH substitution on some layer-silicate minerals. Z Kristallogr Cryst Mater 141(1-2):138-144. https://doi.org/10.1524/zkri.1975.141.1-2.138

Giese RF (1977) The influence of hydroxyl orientation, stacking sequence, and ionic substitutions on the interlayer bonding of micas. Clays Clay Miner

25(2):102-104. https://doi.org/10.1346/CCMN.1977.0250205

Guggenheim S, Zhan W (1998) Effect of temperature on the structures of lizardite-1T and lizardite-2H. Can Mineral 36(6):1587-1594.

Hammerli J, Rubenach M (2018) The role of halogens during regional and contact metamorphism. In: Harlov DE, Aranovich L (eds) The role of halogens in terrestrial and extraterrestrial geochemical processes: surface, crust, and mantle. Springer, Berlin, pp 649-712. https://doi.org/10.1007/978-3-319-61667-4_10

Hanley JJ, Koga TK (2018) Halogens in terrestrial and cosmic geochemical systems: abundances, geochemical behaviors, and analytical methods. In: Harlov DE, Aranovich L (eds) The role of halogens in terrestrial and extraterrestrial geochemical processes: surface, crust, and mantle. Springer, Berlin, pp 21-121. https://doi.org/10.1007/978-3-319-61667-4_2

Hecker JG, Marks MAW, Wenzel T, Markl G (2020) Halogens in amphibole and mica from mantle xenoliths: implications for the halogen distribution and halogen budget of the metasomatized continental lithosphere. Am Mineral 105:781-794. https://doi.org/10.2138/am-2020-7174

Henry DJ, Dutrow BL (2011) The incorporation of fluorine in tourmaline: internal crystallographic controls or external environmental influences? Can Mineral 49(1):41-56. https://doi.org/10.3749/canmin.49.1.41

Henry DJ, Daigle NM (2018) Chlorine incorporation into amphibole and biotite in high-grade iron-formations: interplay between crystallography and metamorphic fluids. Am Mineral 103(1):55-68. https://doi.org/10.2138/am-2018-6143

Ito E, Harris DM, Anderson Jr AT (1983) Alteration of oceanic crust and geologic cycling of chlorine and water. Geochim Cosmochim Acta 47(9):1613-1624. https://doi.org/10.1016/0016-7037(83)90188-6

John T, Scambelluri M, Frische M, Barnes JD, Bach W (2011) Dehydration of subducting serpentinite: implications for halogen mobility in subduction zones and the deep halogen cycle. Earth Planet Sci Lett 308(1-2):65-76. https://doi.org/10.1016/j.epsl.2011.05.038

Juhin A, Calas G, Cabaret D, Galoisy L, Hazemann JL (2008) Structural relaxation around substitutional Cr^{3+} in pyrope garnet. Am Mineral 93(5-6):800-805. https://doi.org/10.2138/am.2008.2823

Lee JH, Guggenheim S (1981) Single crystal X-ray refinement of pyrophyllite-1Tc. Am Mineral 66(3-4):350-357.

Lefeuvre B, Agard P, Verlaguet A, Dubacq B, Plunder A (2020) Massive formation of lawsonite in subducted sediments from the Schistes Lustrés (W. Alps): implications for mass transfer and decarbonation in cold subduction zones. Lithos 370:105629. https://doi.org/10.1016/j.lithos.2020.105629

Lin C, Bailey SW (1984) The crystal structure of paragonite-2M1. Am Mineral 69(1-2):122-127.

Louvel M, Cadoux A, Brooker RA, Proux O, Hazemann JL (2020) New insights on Br speciation in volcanic glasses and structural controls on halogen degassing. Am Mineral 105(6):795-802. https://doi.org/10.1017/S1431927620013495

Luth RW (2003) Mantle volatiles - distribution and consequences. In: Carlson RW (ed) Treatise on Geochemistry, vol 2. Elsevier, Oxford, pp 319-361.

McCarthy MU, Harrison NM (1994) *Ab initio* determination of the bulk properties of MgO. Phys Rev B 49: 8574-8582. https://doi.org/10.1103/PhysRevB.49.8574

Merli M, Ungaretti L, Oberti R (2000) Leverage analysis and structure refinement of minerals. Am Mineral 85(3-4):532-542. https://doi.org/10.2138/am-2000-0415

Mi JX, Pan Y (2018) Halogen-rich minerals: Crystal chemistry and geological significances. In: Harlov DE, Aranovich L (eds) The role of halogens in terrestrial and extraterrestrial geochemical processes: surface, crust, and mantle. Springer, Berlin, pp 123-184. https://doi.org/10.1007/978-3-319-61667-4_3

Morrison J (1991) Compositional constraints on the incorporation of Cl into amphiboles. Am Mineral 76(11-12):1920-1930.

Morse SA (2015) Linear partitioning in binary solutions: a review with a novel partitioning array. Am Mineral 100(5-6):1021-1032. doi:10.1016/j.lithos.2011.11.010

Munoz JL, Ludington S (1977) Fluorine-hydroxyl exchange in synthetic muscovite and its application to muscovite-biotite assemblages. Am Mineral 62(3-4):304-308.

Munoz JL (1984) F-OH and Cl-OH exchange in mica with application to hydrothermal ore deposits. In: Bailey SW (ed) Reviews in Mineralogy: Micas. Rev mineral 13 Mineral Soc Am, Virginia, pp 469-493. https://doi.org/10.1515/9781501508820-015

Nada R, Catlow CRA, Pisani C, Orlando R (1993) An *ab initio* Hartree-Fock perturbed-cluster study of neutral defect in LiF. Model Simul Mat Sci Eng 1:165-187.

Nyfeler D, Armbruster T (1998) Silanol groups in minerals and inorganic compounds. Am Mineral 83(1-2):119-125. https://doi.org/10.2138/am-1998-1-211

Oberti R (1993) The mechanism of Cl incorporation in amphibole. Am Mineral 78(7-8):746-752.

Pabst A (1955) Redescription of the single layer structure of the micas. Am Mineral 40(11-12):967-974.

Pagé L, Hattori K, de Hoog JCM, Okay AI (2016) Halogen (F, Cl, Br, I) behaviour in subducting slabs: a study

of lawsonite blueschists in western Turkey. Earth Planet Sci Lett 442:133-142. https://doi.org/10.1016/j.epsl.2016.02.054

Pagé L, Hattori K (2017) Tracing halogen and B cycling in subduction zones based on obducted, subducted and forearc serpentinites of the Dominican Republic. Sci Rep, 7(1):17776. https://doi.org/10.1038/s41598-017-18139-7

Pagé L, Hattori K, Guillot S (2018) Mantle wedge serpentinites: A transient reservoir of halogens, boron, and nitrogen for the deeper mantle. Geology, 46(10):883-886. https://doi.org/10.1130/G45204.1

Palin EJ, Dove MT, Redfern SAT, Bosenick A, Sainz-Diaz CI, Warren MC (2001) Computational study of tetrahedral Al–Si ordering in muscovite. Phys Chem Mineral 28(8):534-544. https://doi.org/10.1007/s002690100184

Peintinger MF, Vilela Oliveira D, Bredow T (2012) Consistent Gaussian basis sets of triple-zeta valence with polarization quality for solid-state calculations. J Comput Chem 34(6):451-459. https://doi.org/10.1002/jcc.23153

Perdikatsis B, Burzlaff H (1981) Strukturverfeinerung am Talk $Mg_3[(OH)_2Si_4O_{10}]$. Z Kristallogr Cryst Mater 156(3-4):177-186. https://doi.org/10.1524/zkri.1981.156.3-4.177

Ramberg H (1952) Chemical bonds and distribution of cations in silicates. J Geol 60(4):331-355. https://doi.org/10.1086/625982

Robert JL, Beny JM, Ventura GD, Hardy M (1993) Fluorine in micas: crystal-chemical control of the OH-F distribution between trioctahedral and dioctahedral sites. Eur J Mineral 5(1):7-18. https://doi.org/10.1127/ejm/5/1/0007

Robert JL, Kodama H (1988) Generalization of the correlations between hydroxyl-stretching wavenumbers and composition of micas in the system K_2O-MgO-Al_2O_3-SiO_2-H_2O: a single model for trioctahedral and dioctahedral micas. Am J Sci 288:196-212.

Seward TM, Williams-Jones AE, Migdisov AA (2014) The chemistry of metal transport and deposition by ore-forming hydrothermal fluids. In: Holland HD and Turekian KK (eds) Treatise on geochemistry, vol 13. Elsevier, Oxford, pp 29-57. http://dx.doi.org/10.1016/B978-0-08-095975-7.01102-5

Shannon RD (1976) Revised effective ionic radii and systematic studies of interatomic distances in halides and chalcogenides. Acta Crystallogr A 32(5):751-767. https://doi.org/10.1107/S0567739476001551

Siron G, Baumgartner L, Bouvier AS (2018) Significance of OH, F and Cl content in biotite during metamorphism of the Western Adamello contact aureole. Contrib to Mineral Petrol 173(8):1-19. https://doi.org/10.1007/s00410-018-1491-0

Smye AJ, Warren CJ, Bickle MJ (2013) The signature of devolatisation: extraneous 40Ar systematics in high-pressure metamorphic rocks. Geochim Cosmochim Acta 113:94-112. https://doi.org/10.1016/j.gca.2013.03.018

Spandler C, Pirard C (2013) Element recycling from subducting slabs to arc crust: A review. Lithos 170:208-223. https://doi.org/10.1016/j.lithos.2013.02.016

Teiber H, Scharrer M, Marks MAW, Arzamastsev AA, Wenzel T, Markl G (2015) Equilibrium partitioning and subsequent re-distribution of halogens among apatite–biotite–amphibole assemblages from mantle-derived plutonic rocks: Complexities revealed. Lithos, 220:221-237. https://doi.org/10.1016/j.lithos.2015.02.015

Towler MD, Allan NL, Harrison NM, Saunders VR, Mackrodt WC, Aprà E (1994) *Ab initio* study of MnO and NiO. Phys Rev B 50: 5041-5054. https://doi.org/10.1103/PhysRevB.50.5041

Valenzano L, Torres FJ, Doll K, Pascale F, Zicovich-Wilson CM, Dovesi R (2006) *Ab initio* study of the vibrational spectrum and related properties of crystalline compounds; the case of $CaCO_3$ calcite. Z Phys Chem 220:893-912. https://doi.org/10.1524/zpch.2006.220.7.893

Volfinger M, Robert JL, Vielzeuf D, Neiva AMR (1985) Structural control of the chlorine content of OH-bearing silicates (micas and amphiboles). Geochim Cosmochim Acta 49(1):37-48. https://doi.org/10.1016/0016-7037(85)90189-9

Wagner J, Haigis V, Künzel D, Jahn S (2017) Trace element partitioning between silicate melts – A molecular dynamics approach. Geochim Cosmochim Acta 205:245-255. https://doi.org/10.1016/j.gca.2017.02.017

Welch MD, Knight KS (1999) A neutron powder diffraction study of cation ordering in high-temperature synthetic amphiboles. Eur J Mineral, 11(2):321-332. https://doi.org/10.1127/ejm/11/2/0321

Welch MD, Marshall WG (2001) High-pressure behavior of clinochlore. Am Mineral 86(11-12):1380-1386. https://doi.org/10.2138/am-2001-11-1206

Westrich HR (1982) F-OH exchange equilibria between mica-amphibole mineral pairs. Contrib to Mineral Petrol 78(3):318-323. https://doi.org/10.1007/BF00398926

Whitney DL, Evans BW (2010) Abbreviations for names of rock-forming minerals. Am Mineral 95(1):185-187. https://doi.org/10.2138/am.2010.3371

Zellmer GF, Edmonds M, Straub SM (2015) Volatiles in subduction zone magmatism. Geol Soc Spec Publ 410(1):1-17. https://doi.org/10.1144/SP410.13

Figures

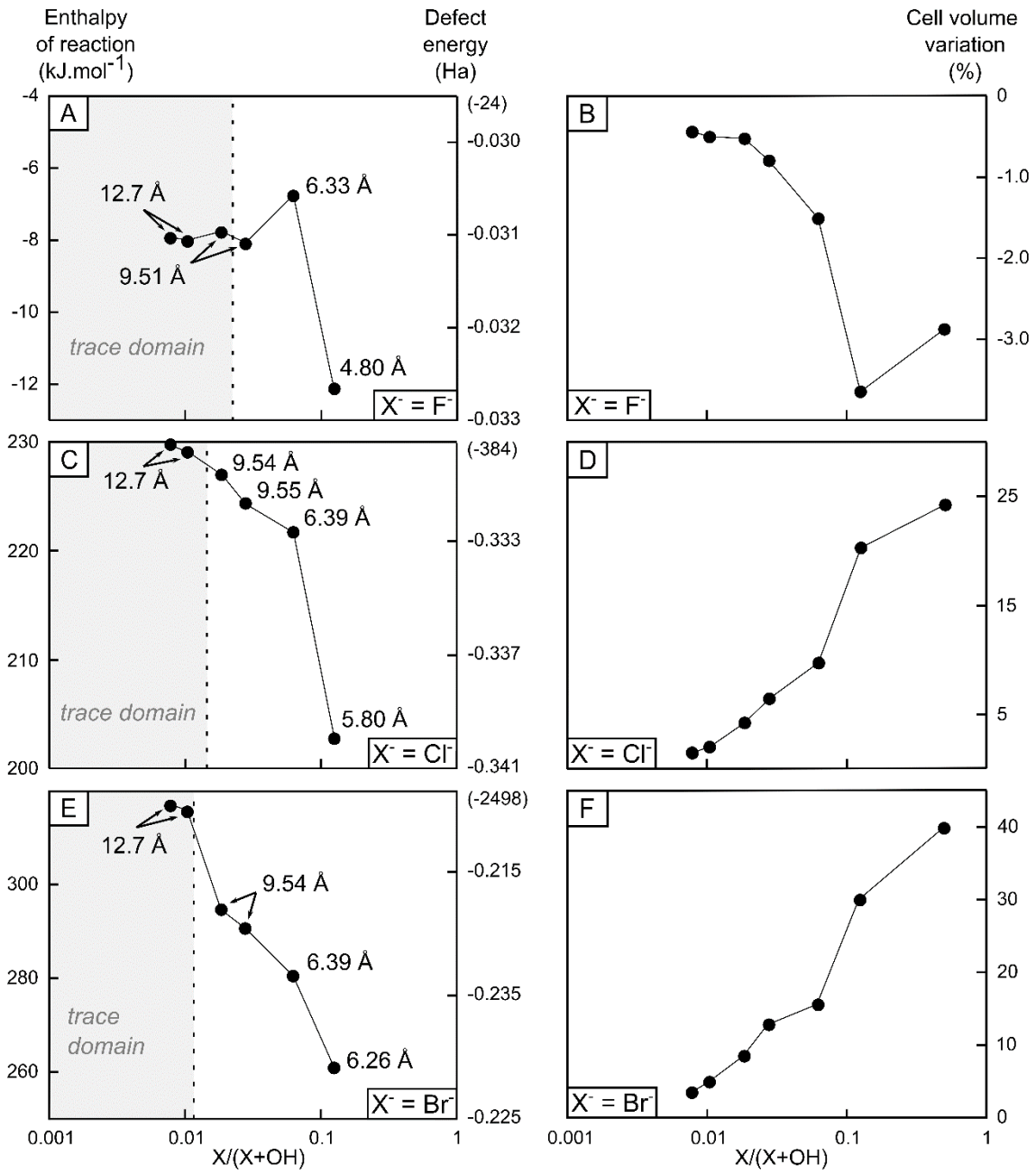

Fig.1: Enthalpies of the exchange reaction with OH^- for F^- (A), Cl^- (C) and Br^- (E) (in $kJ.mol^{-1}$) in brucite shown against halogen concentration. Corresponding defect energies are given on the right-hand side of each graph (in Ha). The shortest distance between two halogen-bearing defects is indicated in Å for each simulation. Cell volume variations compared to brucite are given after exchange of OH^- for F^- (B), Cl^- (D) and Br^- (F). Each halogen exchange is plotted on a different scale. Note that halogen content (x axis) is plotted on log scale.

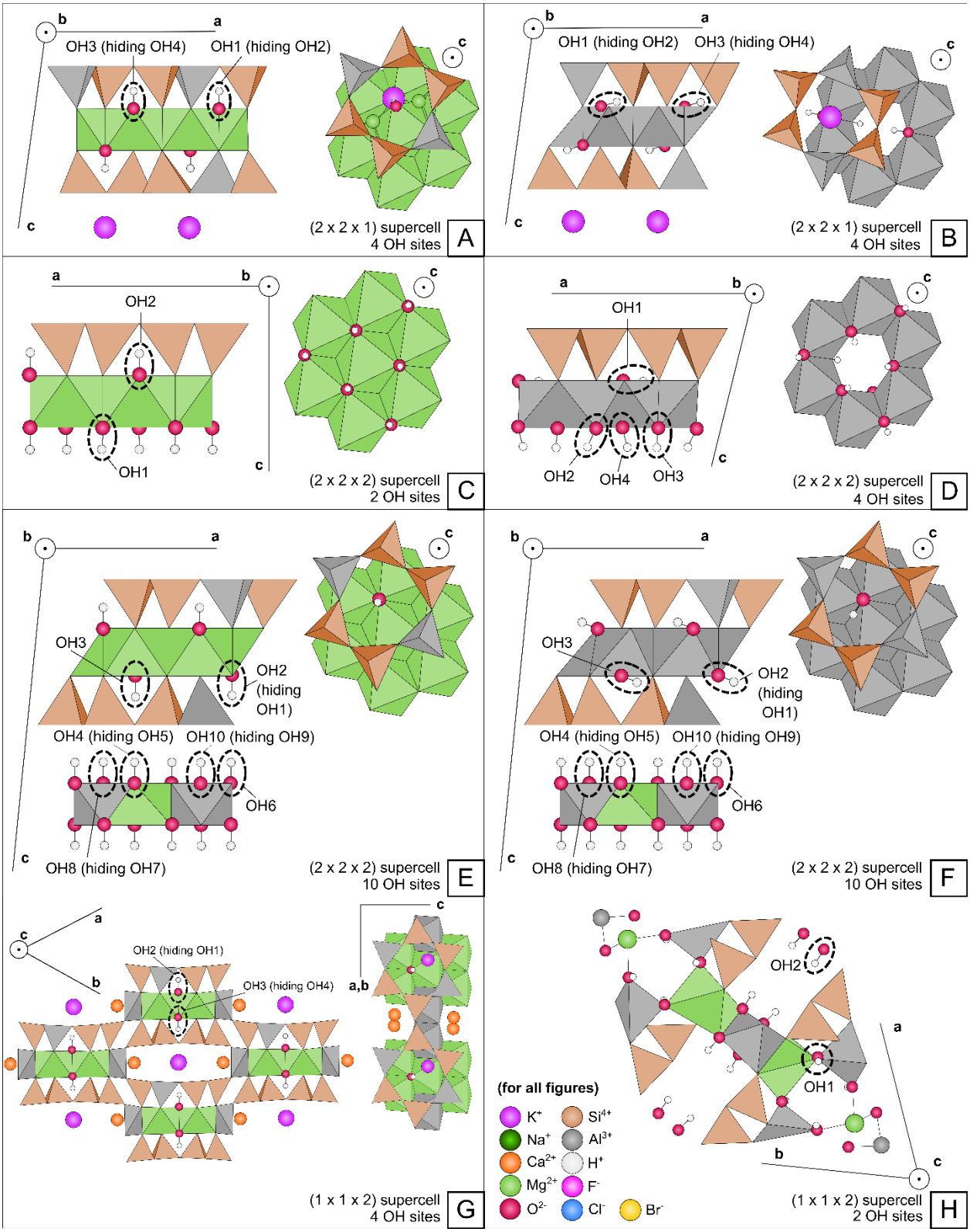

Fig.2: Optimised structures of hydrous silicates displaying several independent OH exchange sites. A) phlogopite, B) muscovite, C) lizardite, D) kaolinite, E) clinochlore, F) sudoite, G) pargasite, H) Mg-carpholite. Epidotes are not shown here because they have only one independent OH site.

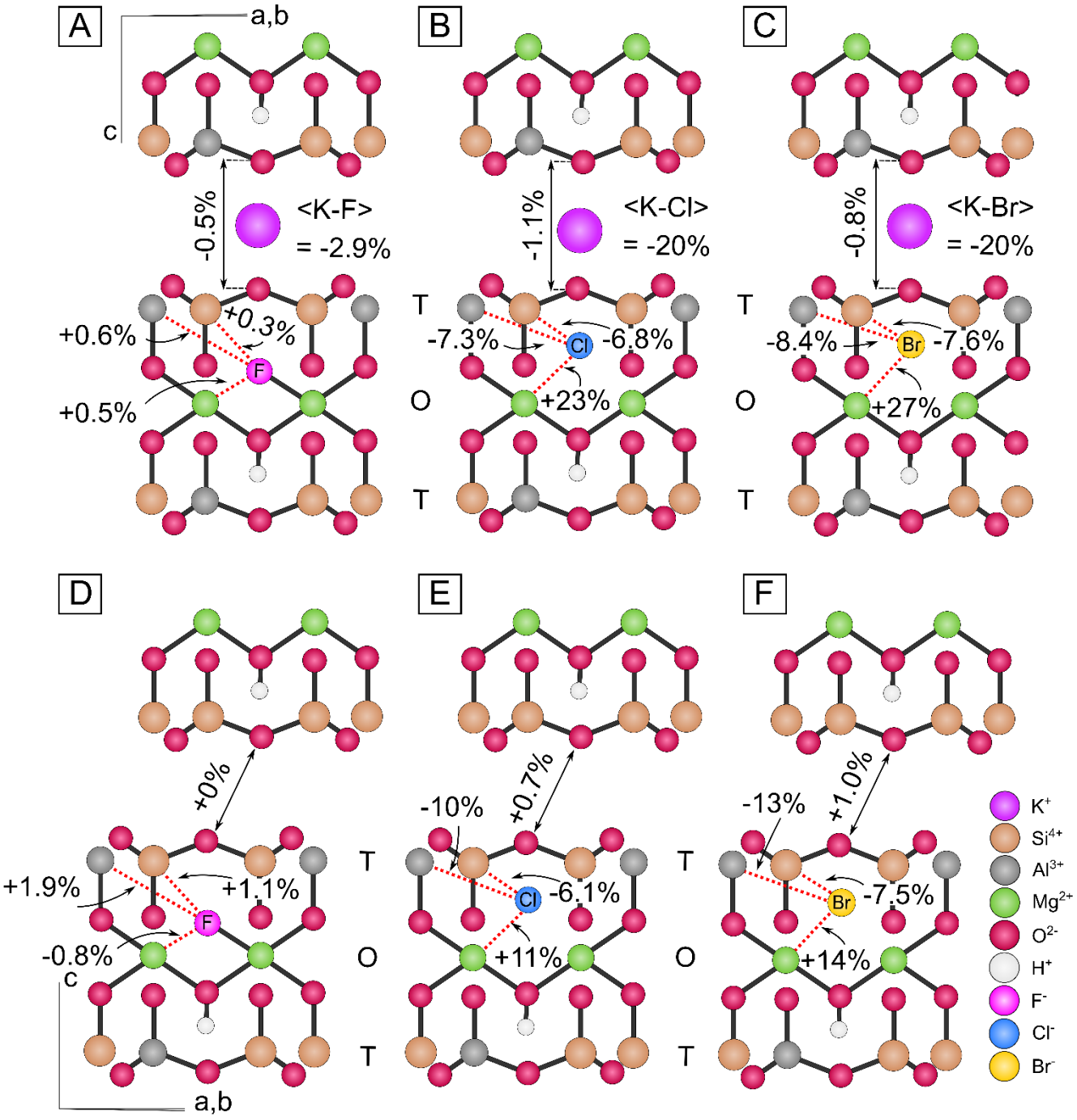

Fig.3: Local strain after halogen incorporation in phlogopite (A, B, C) and talc (D, E, F), in terms of displacement of the halogen from the OH1 site and interatomic distance variations.

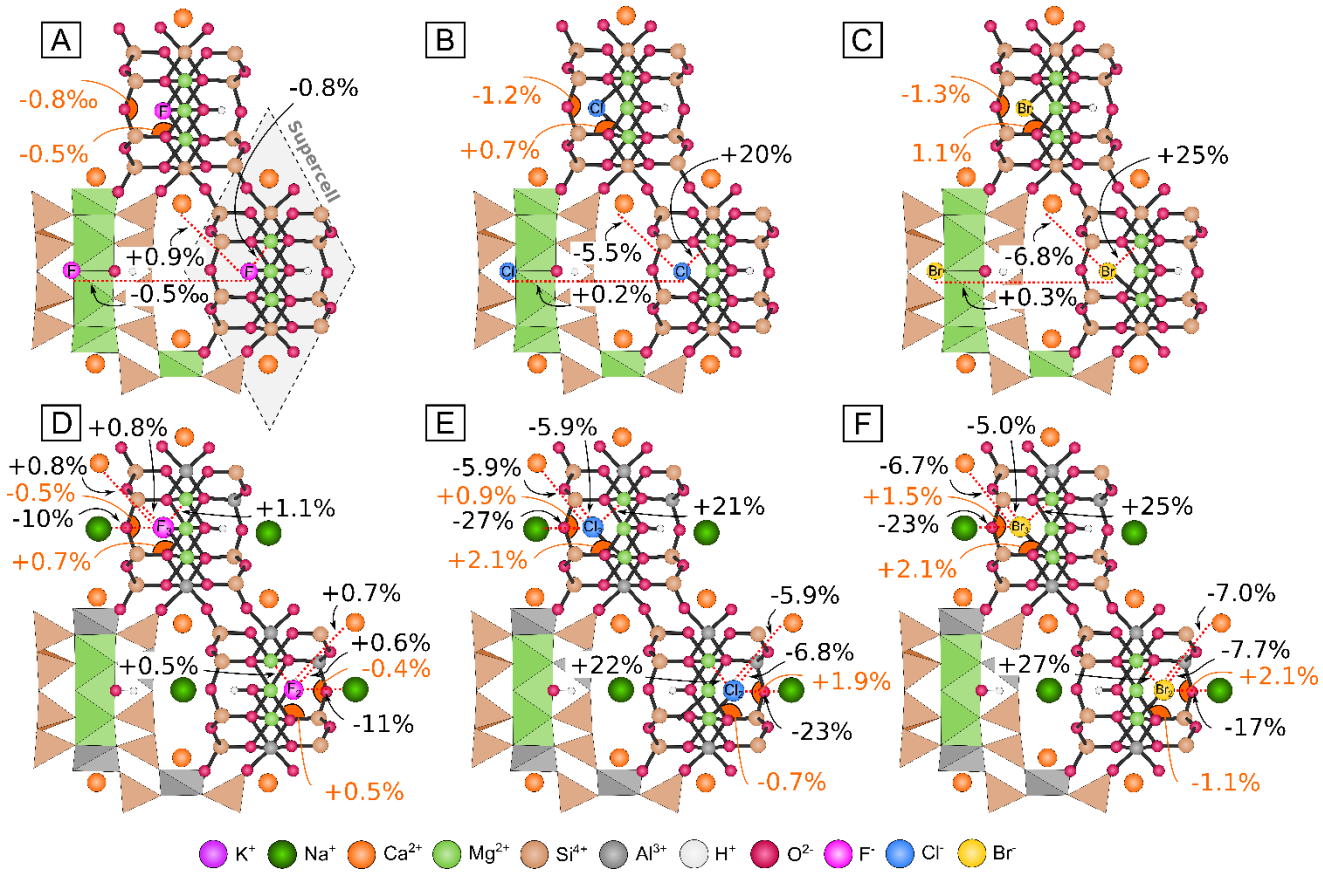

Fig.4: Local strain in tremolite after (A) F uptake, (B) Cl uptake, (C) Br uptake, and in pargasite after (D) F uptake, (E) Cl uptake and (F) Br uptake. Results for pargasite are given for several substitutions, even though each is calculated independently. Strain is indicated in % for distances (in black) and for angles (in orange).

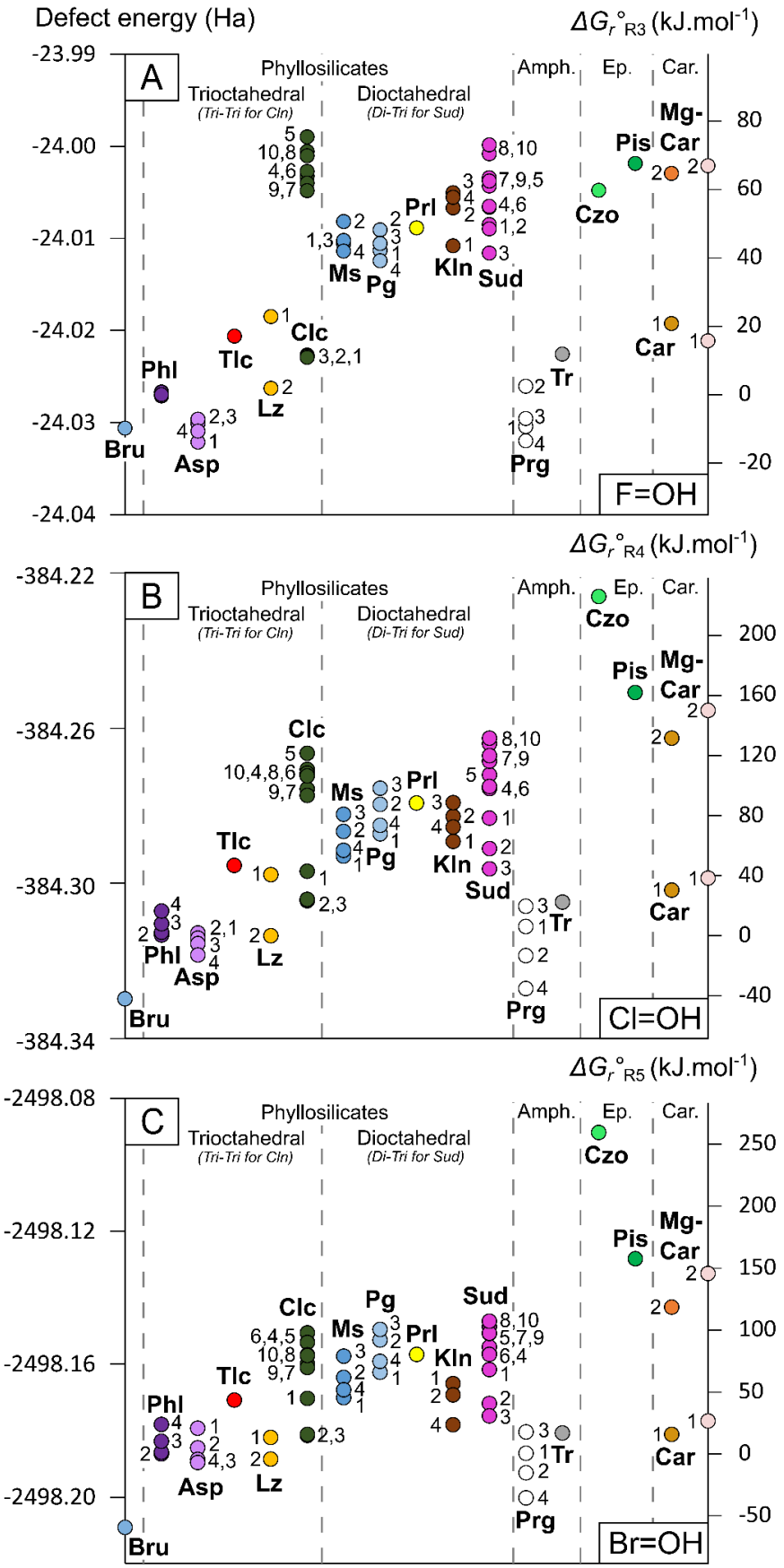

Fig.5: Defect energy (in Ha) for the exchange of OH^- by (A) F^-, (B) Cl^- and (C) Br^-. Numbers indicate OH sites. On the right-hand side, Gibbs free energy of reactions refer to exchange with the OH1 site of phlogopite (in $kJ.mol^{-1}$). They correspond to the difference between the defect energy of $OH1^{Phl}$ and other sites.

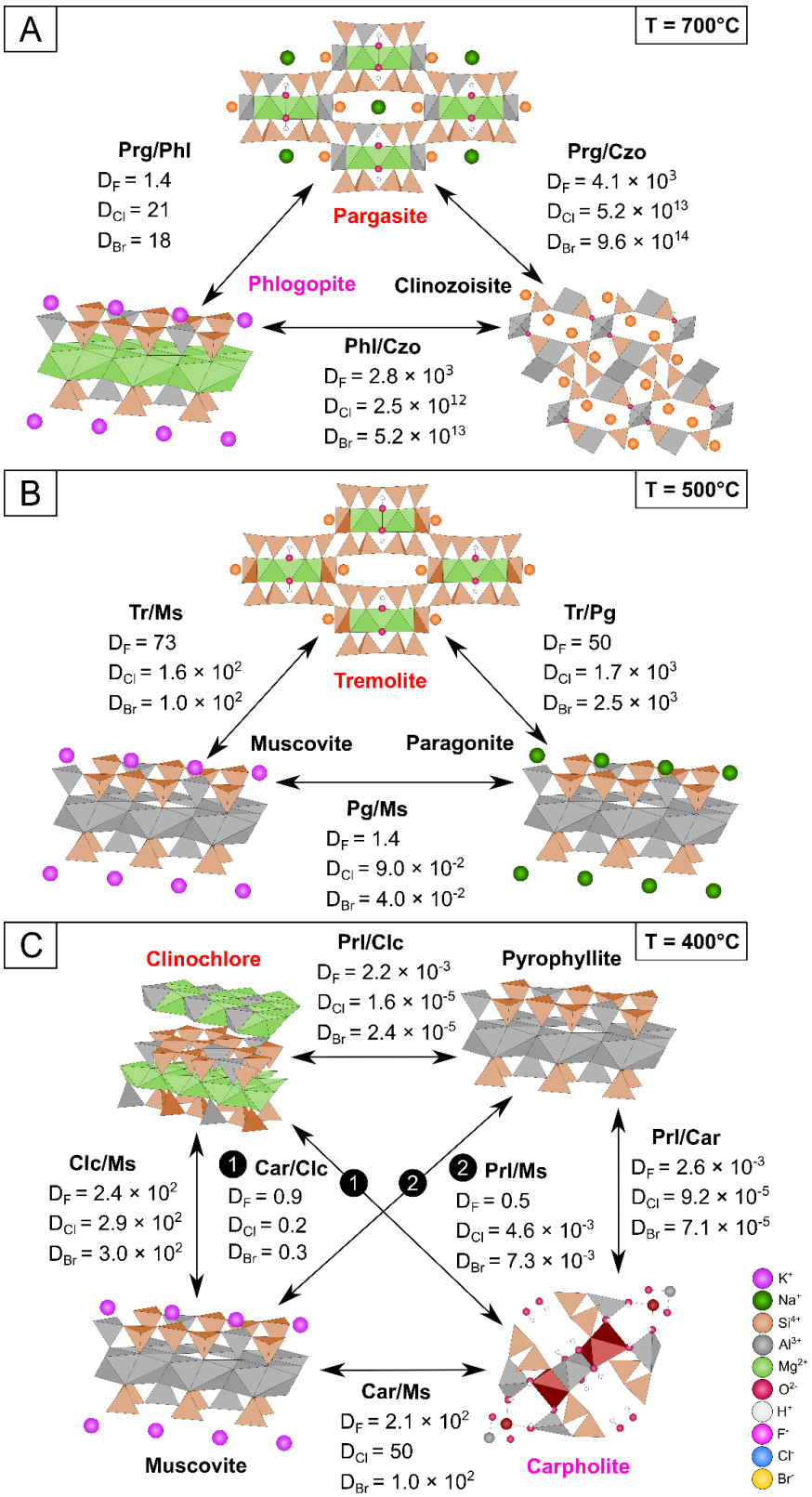

Fig.6: Mass partition coefficients computed for three assemblages at different temperatures: A) pargasite – phlogopite – clinozoisite (700° C), B) tremolite – muscovite – paragonite (500° C) and C) muscovite – clinozoisite – pyrophyllite – Mg-carpholite (400° C). Red labels show the favoured host of halogens in each assemblage, magenta labels show minerals of secondary importance.

Tables

Phase	Formula unit	Supercell ($m \times n \times k$)	Vol. (Å^3)	a (Å)	b (Å)	c (Å)	α (°)	β (°)	γ (°)	Reference
Phlogopite	$KMg_3AlSi_3O_{10}(OH)_2$	2 × 2 × 1	1038.37	10.72	10.72	10.59	85.26	94.83	60.02	
(Phl)		2 × 2 × 1	*980.41*	*10.64*	*10.64*	*10.16*	*85*	*95*	*60.02*	*Pabst (1955)*
Aspidolite	$NaMg_3AlSi_3O_{10}(OH)_2$	2 × 2 × 1	1000	10.76	10.69	10.54	90	104.93	59.83	
(Asp)		2 × 2 × 1	*947.07*	*10.58*	*10.58*	*10.12*	*82.51*	*97.49*	*60.02*	*Banno et al. (2005)*
Muscovite	$KAl_3Si_3O_{10}(OH)_2$	2 × 2 × 1	1959.27	10.5	10.5	20.66	87.15	92.85	59.81	
(Ms)		2 × 2 × 1	*1866.86*	*10.39*	*10.39*	*20.07*	*87.12*	*92.88*	*59.92*	*Catti et al. (1989)*
Paragonite	$NaAl_3Si_3O_{10}(OH)_2$	2 × 2 × 1	1835.78	10.41	10.41	19.61	88.95	91.05	59.76	
(Pg)		2 × 2 × 1	*1755.02*	*10.27*	*10.27*	*19.29*	*87.83*	*92.17*	*59.91*	*Lin and Bailey (1984)*
Talc	$Mg_3Si_4O_{10}(OH)_2$	2 × 2 × 2	1950.94	10.69	10.69	20	85.97	95.57	59.98	
(Tlc)		2 × 2 × 2	*1815.10*	*10.58*	*10.6*	*18.92*	*86.08*	*94.73*	*59.94*	*Perdikatsis and Burzlaff (1981)*
Pyrophyllite	$Al_2Si_4O_{10}(OH)_2$	2 × 2 × 2	1830.67	10.49	10.43	19.68	85.73	95.95	59.81	
(Prl)		2 × 2 × 2	*1700.63*	*10.37*	*10.32*	*18.69*	*85.82*	*96.21*	*59.84*	*Lee and Guggenheim (1981)*
Kaolinite	$Al_2Si_2O_5(OH)_4$	2 × 2 × 2	1373.37	10.47	10.43	15.06	84.33	99.06	59.85	
(Kln)		2 × 2 × 2	*1314.83*	*10.34*	*10.3*	*14.78*	*84.22*	*99.12*	*59.91*	*Bish (1993)*
Lizardite	$Mg_3Si_2O_5(OH)_4$	2 × 2 × 2	1486.90	10.73	10.73	14.91	90	90	120	
(Lz)		2 × 2 × 2	*1486.86*	*10.73*	*10.73*	*14.92*	*90*	*90*	*120*	*Guggenheim and Zhan (1998)*
Clinochlore	$Mg_5Si_3Al_2O_{10}(OH)_8$	2 × 2 × 1	1431.63	10.73	10.73	14.44	86.79	93.21	60.09	
(Clc)		2 × 2 × 1	*1407.05*	*10.65*	*10.65*	*14.41*	*86.47*	*93.53*	*60.06*	*Welch and Marshall (2001)*
Sudoite	$Mg_2Al_3Si_3AlO_{10}(OH)_8$	2 × 2 × 1	1384.13	10.56	10.56	14.36	87.27	92.73	60.32	
(Sud)		2 × 2 × 1	*1346.86*	*10.47*	*10.47*	*14.29*	*86.49*	*93.51*	*60*	*Eggleton and Bailey (1967)*
Pargasite	$NaCa_2Mg_4Al_2(Si_6Al_2)O_{22}(OH)_2$	1 × 1 × 2	934.99	10.32	10.31	10.73	82.95	97.24	57.89	
(Prg)		1 × 1 × 2	*902.82*	*10.24*	*10.24*	*10.56*	*82.58*	*97.42*	*57.76*	*Welch and Knight (1999)*
Tremolite	$Ca_2Mg_5Si_8O_{22}(OH)_2$	1 × 1 × 2	940.67	10.39	10.39	10.68	83.13	96.87	57.47	
(Tr)		1 × 1 × 2	*905.43*	*10.28*	*10.28*	*10.55*	*83*	*97*	*57.19*	*Merli et al. (2000)*
Clinozoisite	$Ca_2Al_3Si_3O_{12}(OH)$	2 × 2 × 2	3733.05	17.85	11.31	20.52	90	115.67	90	
(Czo)		2 × 2 × 2	*3634.88*	*17.76*	*11.17*	*20.31*	*90*	*115.5*	*90*	*Dollase (1968)*
Pistacite	$Ca_2\ Fe^{3+}{}_3Si_3O_{12}(OH)$	2 × 2 × 2	3981.83	18.13	11.72	20.87	90	116.17	90	
(Pis)		2 × 2 × 2	-	-	-	-	-	-	-	
Carpholite	$Mn^{2+}Al_2Si_2O_6(OH)_4$	1 × 1 × 2	1489.67	12.42	12.42	10.36	90	90	68.81	
(Car)		1 × 1 × 2	*1455.76*	*12.35*	*12.35*	*10.29*	*90*	*90*	*68.17*	*Banno et al. (2005)*
Mg-Carpholite	$Mg^{2+}Al_2Si_2O_6(OH)_4$	1 × 1 × 2	1448.70	12.27	12.27	10.32	90	90	68.83	
(MgCar)		1 × 1 × 2	*1407.66*	*12.16*	*12.16*	*10.22*	*90*	*90*	*68.66*	*Fuchs et al. (2001)*

Table 1: Cell parameters and volumes used as inputs (italics) and results of structure optimisation with CRYSTAL17. Factors used to generate supercells along *a*, *b* and *c* axes of the primitive cell are noted *m*, *n* and *k*. Inputs are given in italics. Structures originate from the references given in the table.

	700 °C	**500 °C**	**300 °C**	**300 °C**	**400 °C**	**700 °C**	**400 °C**
F = OH exchange	**Phlogopite**	**Muscovite**	**Lizardite**	**Kaolinite**	**Clinochlore**	**Pargasite**	**Mg-Carpholite**
OH2	1.2	2.7	4.0×10^{-2}	9.5	0.5	4.1	7.5×10^{3}
OH3	1.1	1.2		24	0.9	1.3	
OH4	1.1	0.7		18	9.1×10^{3}	0.6	
OH5					3.3×10^{4}		
OH6					1.1×10^{4}		
OH7					3.2×10^{3}		
OH8					1.6×10^{4}		
OH9					2.1×10^{3}		
OH10					1.3×10^{4}		
Cl = OH exchange					0.5		
OH2	1.3	13	5.2×10^{-4}	35	1.4×10^{-2}	0.3	6.4×10^{8}
OH3	2.5	81		2.5×10^{2}	3.4×10^{-2}	3.9	
OH4	7.3	1.8		8	1.2×10^{5}	2.1×10^{-2}	
OH5					7.7×10^{5}		
OH6					2.2×10^{5}		
OH7					1.1×10^{4}		
OH8					7.2×10^{4}		
OH9					4.9×10^{3}		
OH10					5.1×10^{4}		
Br = OH exchange					1.4×10^{-2}		
OH2	1.2	12	8.5×10^{-2}	0.1	2.7×10^{-3}	0.2	1.1×10^{9}
OH3	3.5	1.7×10^{2}			6.2×10^{-3}	8	
OH4	18	2.6		1.0×10^{-3}	2.8×10^{3}	1.3×10^{-2}	
OH5					5.1×10^{3}		
OH6					2.6×10^{3}		
OH7					64		
OH8					2.3×10^{2}		
OH9					39		
OH10					2.1×10^{2}		

Table 2: Partition coefficients between the OH1 site and the other sites in a single mineral. Computed partition coefficients are given for a representative temperature at which minerals are stable.

Assemblage D: Clc-Phl-Ms - 500° C

	$D^{Phl/Clc}$	$D^{Phl/Ms}$	$D^{Clc/Ms}$
F	7.1	8.1×10^2	1.2×10^2
Cl	36	5.1×10^3	1.4×10^2
Br	9.4	1.4×10^3	1.5×10^2

Assemblage E: Lz-Tlc - 300° C

	$D^{Lz/Tlc}$
F	16
Cl	1.5×10^4
Br	1.3×10^4

Assemblage F: Lz-Kln - 200° C

	$D^{Lz/Kln}$
F	2.6×10^4
Cl	9.7×10^6
Br	9.0×10^2

Table 3: Mass partition coefficients computed for three theoretical assemblages at different temperatures: clinochlore – phlogopite – muscovite (500° C), lizardite – talc (300° C) and lizardite – kaolinite (200° C).